This manuscript is a preprint and has been accepted for publication in the **Journal of Structural Geology**. This manuscript version has not undergone proof read.
The final version of this manuscript will be available on the journals system at https://doi.org/10.1016/j.jsg.2021.104463 (*open access*). Please use this DOI for any future referring.

Microstructure and fluid flow in the vicinity of basin bounding faults in rifts – the Dombjerg Fault, NE Greenland rift system

Eric Salomon[1,2,*], Atle Rotevatn[1], Thomas Berg Kristensen[1,3], Sten-Andreas Grundvåg[4], Gijs Allard Henstra[1,5]

[1]Department of Earth Science, University of Bergen, Bergen, Norway

[2]now at GeoZentrum Nordbayern, University of Erlangen-Nuremberg, Erlangen, Germany

[3]now at Equinor ASA, Bergen, Norway

[4]Department of Geosciences, UiT The Arctic University of Norway, Tromsø, Norway

[5]now at AkerBP, Fornebu, Norway

*corresponding author (e.salomon@outlook.de, +49 9131 85 25915)

Abstract

Faults commonly form loci for high fluid flux in sedimentary basins, where fluids, rocks and deformation processes frequently interact. Here, we elucidate the interaction of fluid flow, diagenesis and deformation near basin-bounding faults in sedimentary basins through a study in the vicinity (0-3.5 km) of the Dombjerg Fault in the NE Greenland rift system. Due to fault-controlled fluid circulation, fault-proximal syn-rift clastics underwent pervasive calcite cementation, whereas uncemented clastics at some distance from the fault remained highly porous and friable. Correspondingly, two distinct deformation regimes

developed to accommodate continued deformation: discrete brittle fractures formed in calcite cemented rocks, whereas cataclastic deformation bands formed in uncemented deposits.

We show that low-permeable deformation bands forming in highly porous rocks were associated with localized host rock alteration, and chemical reduction of porosity along bands. In rocks with cementation-induced low porosity, brittle fractures created new pathways for fluids, but were subsequently filled with calcite. Occasionally, veins comprise multiple generations of microcrystalline calcite, likely precipitated from rapidly super-saturated fluids injected into the fractures. This suggests cemented deposits sealed uncemented compartments, where fluid overpressure developed. We conclude that compartmentalized flow regimes may form in fault-bounded basins, which has wide implications for assessments of potential carbon storage, hydrocarbon, groundwater, and geothermal sites.

Keywords: syn-rift, fluid flow, fault evolution, structural diagenesis, fracturing, cementation

1. Introduction

Deformation, fluid flow and diagenesis are strongly interactive processes that determine the evolution and properties of clastic sediments and rocks during and following deposition (e.g., Knipe, 1993; Laubach et al., 2010). For example, the style and mechanisms of deformation are highly dependent on the diagenetic state of such host rocks. In unconsolidated and/or poorly lithified, highly porous granular rocks, deformation is commonly accommodated by grain reorganization or crushing that often result in the formation of deformation bands (e.g., Mandl et al., 1977; Aydin, 1978; Rawling and Goodwin, 2003; Fossen et al., 2018, and references therein). Fluids flow through open pore space in such sedimentary rock and may locally be guided by deformation bands or other

heterogeneities such as stratification (e.g., Antonellini and Aydin, 1994; Philipps, 2009; Balsamo et al., 2012; Del Sole et al., 2020; Dimmen et al., 2020). Increasing compaction and cementation leads to a reduction of porosity and permeability (e.g., Houseknecht, 1987; Lundegard, 1992; Pizzati et al., 2020), while at the same time to an increase of the tensile strength of the rock (e.g., Dyke and Dobereiner, 1991; Cook et al., 2015). The latter promotes a transition from grain scale deformation processes of particulate/granular and cataclastic flow processes (see e.g. Menéndez et al., 1996; Rawling and Goodwin, 2003) to discrete brittle failure, with fracture formation providing new pathways for fluids (e.g., Fisher et al., 2003; Williams et al., 2017). In turn, pore fluids may, for example, promote cementation, slow the rate of compaction, or be responsible for the creation of secondary porosity, depending on their pressure and composition (e.g., Bjørlykke, 1988; Taylor et al., 2010).

In general, diagenesis of clastic sediments is a function of temperature, burial pressure, and fluid and sediment chemistry (e.g., Bjørlykke, 1988; Worden and Burley, 2003). The presence/development of faults may significantly affect these processes e.g. by influencing heat flow (e.g., Bellani et al., 2004; Townend et al., 2017; Vanneste et al., 2005) and fluid circulation (e.g., Gibson, 1998; Eichhubl and Boles, 2000; Balsamo et al., 2013; Bense et al., 2013). The results of such influence have been showcased along the Dombjerg Fault, a major basin-bounding fault in NE Greenland rift system (Kristensen et al., 2016; Salomon et al., 2020; Fig. 1). Here, syn-rift siliciclastic deposits in the hanging wall, juxtaposed against a footwall of crystalline basement, are affected by pervasive fault-proximal calcite cementation, which is interpreted to have resulted from fault-controlled fluid flow and diagenesis.

Previously, Kristensen et al. (2016) have given an overview over the overall structure of the Dombjerg Fault damage zone, and Salomon et al. (2020) analyzed the related fault-controlled diagenetic history and paragenesis. Building on these previous works we here elucidate the effect of this structural and diagenetic evolution on the ensuing fluid flow and

deformation history following the establishment of a calcite-cemented zone in the hanging wall of the Dombjerg Fault. The overarching aim of this study is to understand the effects of interaction of deformation, fluid flow and diagenesis operating in the proximity of large, basin-bounding fault systems in rift basins. More specifically, we here aim to understand how these fault-to-basin-scale processes are reflected on a microstructural scale. The work is based on microstructural analyses of the main deformation structures occurring within a distance of 0-3.5 km of the fault, i.e. veins within the calcite cementation zone, and deformation bands in the uncemented clastic deposits outside the cementation zone. We show that deformation bands acted as local baffles to fluid flow, while cementation created compartments of fluid overpressure that was repeatedly released upon fracturing.

2. Geological Setting

The East Greenland rift system is a long-lived rift system whose formation initiated in the Devonian and which was active episodically throughout Paleozoic and Mesozoic times, until continental breakup and opening of the North Atlantic in the Early Eocene times (e.g., Larsen and Watt, 1985; Surlyk, 1990; Stemmerik et al., 1991; Rotevatn et al., 2018). The rift system is exposed onshore East Greenland along the coast between 68-77°N (Henriksen, 2003; fig. 1a). It is characterized by a right-stepping N-S to NNW-SSE trending border fault network, with segment lengths of 170-230 km (Fig. 1a) and with vertical throws up to ~5 km (Surlyk, 2003).

The Dombjerg Fault is part of this border fault system and marks the western margin of the Wollaston Forland Basin (Fig. 1b). Activity of the fault started in the Carboniferous (Rotevatn et al., 2018) and culminated in a main rift phase in the Late Jurassic / Early Cretaceous (e.g., Surlyk, 1984) at which time the Wollaston Forland Basin was established as

a syn-rift half-graben depocentre east of the fault (cf. Gawthorpe and Leeder, 2000). The infill of this half-graben basin can be subdivided into stages of early syn-rift, rift climax, and late syn-rift deposits (sensu Surlyk and Korstgård, 2013; Prosser, 1993). Early syn-rift deposits of Middle to Late Jurassic age are represented by marine sandstones with thin interlayers of mudstone (i.e. Vardekløft and Hall Bredning Groups; fig. 1b; Surlyk and Korstgård, 2013). Rift climax and late syn-rift deposits of Late Jurassic to Early Cretaceous age are assigned to the Wollaston Forland Group, an up to ~3 km thick clastic succession. The lower part of the succession consists predominantly of sandstones and conglomerates that were emplaced by fully submarine gravity flows (Lindemans Bugt Formation; rift climax; Henstra el al., 2016), whereas the succeeding part consists of marine sandstones and conglomerates interfingering with marine mudstones and carbonates (Palnatokes Bjerg Formation; late syn-rift; fig. 1b, Surlyk and Korstgård, 2013).

Of main relevance for this study is the Lindemans Bugt Formation, which forms a clastic wedge that is bounded by the Dombjerg Fault in the west and is gradually thinning eastward into the basin over a distance of 10-15 km (Fig. 1c; Henstra et al., 2016). The deposits of this unit are the erosional products derived from the footwall, which consists for the most part of Caledonian crystalline basement, and were transported as rock falls, debris flows, and turbidity currents into a deep-marine rift basin environment in the hanging wall (Fig. 1; Henstra et al., 2016).

Kristensen et al. (2016) and Salomon et al. (2020) have previously described the diagenetic and deformational character of the rift-climax deep-water clastic deposits of the Lindemans Bugt Formation. We here provide a summary of their main findings as context for the present study. The fault-proximal deposits of the Lindemans Bugt Formation were extensively cemented by calcite within a zone of up to ~1.5 km width into the hanging wall from the fault (Kristensen et al., 2016; Salomon et al., 2020; figs. 2, 3). Close to the fault,

cementation is pervasive in the hanging wall deposits, though some beds and intervals remain uncemented (Fig. 3c). Towards the fault-distal margin of the cementation zone, the amount of calcite cement decreases. Here, calcite cement is irregularly distributed within beds, leaving uncemented bodies enclosed by cemented strata (Figs. 3a,b; Salomon et al. 2020). Farther eastward into the basin and outside the cementation zone, calcite cement is confined to selected conglomerate beds only.

Overall, calcite cement pervasively fills intergranular space, which reduces the porosity of the affected deposits towards zero (Salomon et al., 2020) and results in a high competence contrast of the rock relative to the uncemented deposits, which remain porous and friable (Figs. 3a-c). Calcite cementation started shortly after deposition of the clastic sediments during the rift climax in the Valanginian at temperatures between ~30-70°C and an estimated burial depth of < 1 km (Salomon et al., 2020). Calcite veins, which cut through the cemented rock, formed within a similar temperature range, but predominantly in the post-rift phase in the Aptian/Albian (Salomon et al., 2020).

The Dombjerg Fault damage zone affects the Lindemans Bugt Formation up to ~500 m into the hanging wall (Kristensen et al., 2016). In fault-proximal outcrops (~100 m from the fault), calcite veins and joints occur at densities of ~7 veins/joints per meter; rarely, minor faults of <10 cm normal displacement are present. Towards the distal parts of the hanging wall damage zone, the vein and joint density decreases to 4 joints/m and 1 calcite vein/m (Kristensen et al., 2016; in the present study, we find similar densities also in outcrops ~1.4 km away from the fault). Joints consistently overprint veins. Where uncemented, the clastic sedimentary rock hosts deformation bands, while veins are absent. These deformation bands occurring outside the cementation zone, and the veins occurring within this zone, form the focus of the present study.

3. Methodology

The study is based on a suite of samples acquired from the Dombjerg Fault hanging wall damage zone during a three-week field season in the summer of 2018. The samples were collected from sedimentary rocks in a transect extending from the fault and up to c. 3.5 km into the hanging wall. The samples comprise veins, deformation bands, and their associated wall/host rocks. In total, we obtained samples for 14 thin sections of calcite veins cutting through cemented sandstones and conglomerates within the cementation zone most proximal to the fault (within c. 1.5 km distance from the fault). Sampling of deformation bands was challenging due to the friable state of the rocks outside the cementation zone; however, a total of 5 thin sections of deformation bands were successfully prepared. Thin sections were analyzed using a Keyence VHX digital optical microscope, a Technosyn 8200Mk II for cold-cathode cathodoluminescence, and Zeiss Supra 55VP and Hitachi TM4000plus scanning electron microscopes for BSE, EDX, and SEM-cathodoluminescence analyses. The two-dimensional porosity of the samples was determined by image analyses of BSE images mosaics using Adobe Photoshop. Previously obtained formation ages and temperatures of calcite veins and cements (based on U-Pb calcite dating and clumped isotope analysis; see Salomon et al., 2020) provide time constraints on the studied cements and vein fills. In addition, oxygen and carbon isotope data of Salomon et al. (2020) provide information on fluid source for the vein fill, which is complemented here by $\delta^{13}C$ measurements of six additional vein fill generation. Carbon isotopes were analyzed by reaction of carbonate powders with 100% phosphoric acid at 70°C using a Gasbench II connected to a ThermoFisher Delta V Plus mass spectrometer. Reproducibility and accuracy was monitored by replicate analysis of laboratory standards calibrated by assigning a $\delta^{13}C$ of +1.95‰ to NBS19 and -47.3‰ to IAEACO9 and was ± 0.07 ‰ (1 std. dev.).

4. Results

4.1 Deformation band characteristics

Deformation bands occur in the uncemented deposits outside the cementation zone, and within uncemented bodies of sedimentary rock inside the cementation zone (Figs. 2, 4); deformation bands are absent in the cemented deposits within the cementation zone. The overall trend of the deformation bands is E-NE and thus roughly similar to the orientation of the veins in the cemented deposits, with the caveat that this observation is based on a limited number of bands (n = 17; fig. 2). In outcrop location 20 (Fig. 2), NE-trending deformation bands cross-cut an older set of NW-trending bands. This NW-trend is also present in a minor set of veins in the nearby location 18 (Fig. 2), although an age relationship between the two vein sets could not be established. One normal fault (Fig. 4f), also NE-trending, was found outside the cementation zone, which is visible in two outcrops ~20 m apart from each other. In one of these, the fault comprises a 25 cm-wide breccia zone (Fig. 4f), while in the second outcrop, this zone is splayed into a ~40 cm-wide cluster of deformation bands (≥ 6 bands), some of which exhibit slickenside surfaces (Fig. 4e). Slickensides indicate normal throw to the NW (see rose plot Loc. 26 in figure 2). Fault offset clearly exceeds the vertical extent of the outcrop (5 m), as there are distinct marker horizons, but which in the hanging wall are downthrown to below the level of the exposure (samples from this fault are described below).

Deformation band samples are taken from outcrop locations 22 (sample G-48), 23 (samples G-49, G-50), and 26 (samples G-57, G-60), thus from outside the cementation zone (Fig. 2). Samples G-57 and G-60 are derived from the fault described above; G-57 is from the deformation band cluster and G-60 from the center of the breccia zone (Fig. 4f). All deformation bands occur in angular-grained, moderately sorted, fine- to very coarse-grained sub-arkosic sandstone. The fault, represented by sample G-60, also cuts through matrix-supported conglomerate. The sampled bands have an overall strike of E to NE with dip angles

between 70-81° (Figs. 4b-f). The amount of offset along the bands could only be determined for samples G-49 and G-50, which exhibit ~5 cm and ~1-2 cm of normal displacement, respectively.

The deformation bands appear slightly variable across the sample suit. Sample G-48 hosts a ~12.5 mm-wide deformation band that, in the thin section, is hard to differentiate from the host rock. The boundary is gradual and the band itself is characterized by a subtle reduction in grain size relative to the host rock, which we attribute to cataclasis (Fig. 5a). The ~15 mm-wide deformation band in sample G-49 has a subtle boundary to the host rock, as well, and hosts a matrix of crushed material and is clast-supported (Fig. 5b). Traces of brownish coloration within the band can be attributed to fragmented biotite flakes. Sample G-50 hosts a ~1.5-3.0 mm-wide deformation band with a boundary to the wall rock that is more distinct, indicated by a strong brown coloration of the wall rock and a band with a high amount of crushed grains forming a matrix-supported structure (Figs. 5c,d). Similar characteristics apply to sample G-57, with the distinction that the thin section hosts an array of three ~2-4 mm wide deformation bands, that are separated by ~2.0-3.5 mm wide zones of compacted wall rock (Figs. 5e,f). G-60 exhibits across the whole thin section intense grain fracturing due to cataclasis, yet a large quantity of intact clasts are present as well (Figs. 5g,h).

4.2 Alteration associated with deformation bands

The sandstone hosting the deformation bands is altered at a varying degree that is expressed in outcrops by a coloration from light grey (seemingly unaltered state) to dark red. While a yellow coloration seems to have formed independently from deformation bands (Figs. 4a,b,f), a red coloration appears to be confined to the bands. Along the band represented by sample G-49 (Fig. 4c), the footwall host rock has a dominant red coloration which is present across the whole length of the footwall's exposure in the outcrop (~5 m).

Along the band represented by sample G-57 (Fig. 4e), the red coloration covers a ~5-30 cm wide zone of footwall host rock and fades into a light grey color farther into the footwall, which is also the dominant coloration of the hanging wall. In addition, in the cases of the bands shown in figures 4c and 4d and represented by samples G-49 and G-50, a dark red~1 cm-wide rim occurs along both sides of the bands. In two occasions (Figs. 4c,d), the deformation bands splay and enclose a section of light grey host rock.

While the yellow coloration presumably derives from the alteration of feldspar, the dark red coloration is caused by the precipitation of Fe-/Ti-oxides and jarosite (Fig. 6). Oxides are abundant as rims between the lamellae of biotite flakes and in pore space and grain boundaries surrounding the mica. Jarosite appears as a fine mass in the vicinity to mica flakes although rarely in between mica lamellae (Fig. 6i; EDX spectra and element maps in supplements). A clear age relationship between oxide and jarosite formation could not be established from the thin section analysis. With distance to the deformation band the degree of biotite alteration declines and the presence of oxides and jarosite is commonly confined to parts of expanded/deformed flakes of biotite (Figs. 6f,g). Within the deformation bands, biotite is highly deformed yet unaltered and oxides/jarosite nearly completely absent (Figs. 6b,c).

4.3 Deformation band porosity analysis

We created BSE image mosaics for 2-D porosity image analysis of the five deformation band samples (Fig. 7, table 1). In sample G-48, the wall rock has a porosity of 21.9 % and the deformation band 14.9 %. Sample G-49 yields a wall rock porosity of 18.5 %, a deformation band porosity of 7.1 %, and a porosity in the red-stained zone of 5.2 %. In sample G-50, the wall rock has a porosity of 25.8 %, the deformation band 13.6 %, and the red-stained zone along the band 11.8 %. Sample G-57 hosts three single deformation bands

with porosities of 8.0 %, 9.0 %, 9.1 %, respectively, while the slightly reddish altered wall rock has 17.6 % porosity (Fig. 7). Sample G-58, which has been taken ~20 cm away from this band cluster in the more whitish rock (Figs. 4e, 7), the porosity is slightly higher with 21.6 %. We note that all values should only be taken as a rough measure and may be overestimated (e.g., especially sample G-50 suffered from expansion during the epoxy impregnation due to its incohesive condition); however, we are interested in the relative differences rather than the exact values. Summarized, the deformation bands all exhibit lower porosity than their host rocks. Red-stained alteration zones, on the other hand, show somewhat variable porosity.

4.4 Calcite vein characteristics

The cemented deposits are dissected by calcite veins with an overall N-NE trend (Figs. 2, 8), i.e. oblique to the trend of the Dombjerg Fault (NNW-trending; fig. 2). Since most outcrops were exposed in 3-D, we regard this overall trend as unbiased by outcrop orientation. Vein thicknesses range from sub-millimetric to c. 7 cm. All analyzed veins exhibit at least one generation of elongate to blocky syntaxial crystal growth. Separate phases of vein growth are visible in two-thirds of the samples and distinguishable by variable quantities of dust or iron-oxide inclusions (Figs. 9a-d). Crack-seal events are present in 12 of the 14 samples and commonly occur at the contact of vein and wall rock, but occasionally breach through existing vein generations. In all crack-seal events, the younger vein generation does not exceed in thickness the initial vein generation. The majority of veins exhibit opening-mode displacement, while slip zones within the veins are found in three of the 14 samples (Figs. 9g,h).

In outcrop locations 4 and 17, situated approximately 500 m and 1400 m away from the fault into the hanging wall, respectively, a distinctively different vein fill is visible, which appears as an opaque, brownish to greyish calcite matrix that hosts sediment grains (Figs. 8b-

e). In thin section view of samples G-9, G-10, G-13 (all from location 4; fig. 2), and G-37 (location 17), this vein fill identifies as multiple generations of microcrystalline calcite with calcite crystal sizes <10 µm that precede the blocky/elongate crystal growth (Figs. 9e,f, 10). In the thin section of sample G-9 (Figs. 8b, 10a-c), taken from a vertical oriented face, the following characteristics stand out:

- A repetitive infill is observable: Quartz, feldspar, and other clasts as well as lithic fragments of cemented wall rock and of earlier vein generations are localized in a matrix of microcrystalline calcite at the bottom of each infill generation (c.f. point 4 in figure 10b). Upward, these components decrease in grain size and mica flakes become the dominant clast type. The remaining upper part of each section consists nearly exclusively of microcrystalline calcite.
- Older vein generations are brecciated, with brecciated fragments consisting of pure microcrystalline calcite or microcrystalline calcite-hosting clasts (c.f. point 2 in figure 10a).
- In at least one generation, mica flakes are aligned parallel to each other with their overall orientation guided by the outline of older vein generations (point 6 in figure 10c).
- In the central section of the vein, a series of thin (<0.5 mm) veins exists with blocky/elongate calcite crystals. These veins align parallel to an anastomosing set of thin (<0.05 mm), dark bands within the microcrystalline calcite (point 5 in figure 10b).

Sample G-37 derives from a fracture, in which the microcrystalline infill is visible from the base of its outcrop exposure upwards over ~50 cm where it is in contact with elongate calcite crystals (Fig. 8e), which fill the remaining upper section of the fracture as far

as exposed. In addition, a crack-seal elongate/blocky calcite vein generation has formed along the microcrystalline infill and wall rock (Fig. 8e). In the thin section of sample G-37, multiple generations of upward-fining vein fill are present, similar to the composition and texture in sample G-9 (point 7 in figure 10e). A notable difference to sample G-9 is the absence of crack-seal events with the repeated sealing with microcrystalline calcite. The vein of sample G-13, traceable in the outcrop only on a horizontal surface, comprises a horizontal transition of an elongate calcite vein to microcrystalline calcite hosting sediment grains (Fig. 10f).

Carbonate $\delta^{13}C_{VPDB}$ values measured of six microcrystalline vein generations range from -17.9 to -13.2 ‰ (average -14.8 ‰; table 2).

5. Discussion

5.1 Deformation band structure

Deformation bands are exclusively found in host rocks absent of calcite cement in outcrops both within (in uncemented bodies) and outside the cementation zone; however, no deformation bands are found within cemented deposits, suggesting that the bands likely formed *after* calcite cementation and establishment of the wider cementation zone. We do, for example, not find any deformation bands overprinted by calcite cementation, which further strengthens the hypothesis that calcite cementation pre-dates the formation of deformation bands. Furthermore, the overall orientation of the bands is approximately parallel to the general trend of calcite veins (Fig. 2), which suggests they formed in the same stress system. The majority of veins have been dated to the Aptian/Albian (~123-104 Ma), coinciding with an extension phase from latest Valanginian to middle Albian times (Salomon et al., 2020; see also chapter 5.3).

All sampled deformation bands show a cataclastic reduction of grain size, a mechanism that is seen as the key-controlling factor to reduce porosity and permeability in deformation bands (e.g., Pittman, 1981; Antonellini et al., 1994; Ballas et al., 2015). Compared to the mostly unaltered wall rock, porosity within the deformation bands is reduced by approximately one to two thirds (Fig. 7, table 1), which is well within the range of reported porosity losses from host rock to cataclastic deformation bands elsewhere (e.g., Aydin and Johnson, 1983; Antonellini and Aydin, 1994; Torabi and Fossen, 2009).

5.2 Alteration along deformation bands

At the outcrop scale, three of the analyzed five deformation bands exhibit a control on the degree of host rock alteration. This is indicated by the sharp transition across the band from a yellow/white-colored hanging wall to a red-colored footwall (Figs. 4c,e; represented by samples G-49, G-57) as well as by the unaltered host rock enclosed by splaying deformation bands (Figs. 4c,d; samples G-49, G-50). Such alteration effects along deformation bands have been reported before by others and have been attributed to a control of the bands on local fluid flow (e.g., Exner and Tschegg, 2012; Ballas et al., 2012; Dimmen et al. 2020), and it is widely recognized that deformation bands may act as local baffles to flow due to the porosity and permeability reduction in the bands (e.g., Antonellini and Aydin, 1995; Rotevatn et al., 2009; Torabi et al., 2013; Philit et al., 2019).

A clear trend between porosity and degree of host rock alteration is not visible in our dataset. In outcrop location 23, the deformation bands represented by samples G-49 and G-50 yield porosity values of 7.1 % and 13.6 %, respectively. Here, only the low-porosity band of G-50 shows a significant control on footwall alteration (Fig. 4c). Nevertheless, the high-porosity band of G-49 encloses unaltered host rock in a splay zone (Fig. 4d), showcasing the band's potential to also affect host rock alteration. In outcrop location 25, samples G-57 and

G-60 derive from the same fault and yield similar porosity values of ~8-9 %, yet alteration only occurs at the site of G-57 (Figs. 4e,f).

Hence, porosity values determined from single samples and the degree of alteration should not immediately be taken as indicators for the bands impact on fluid flow. It has been shown that porosity can be highly variable laterally within a band at a very local scale (Fossen and Bale, 2007; Torabi and Fossen, 2009). The degree of cataclasis, i.e. the main contributor to porosity reduction (e.g., Pittman, 1981; Antonellini et al.., 1994; Ballas et al., 2015), is partially controlled by the host rock composition and grain properties, e.g. grain sorting, roundness, or mineralogy (e.g., Cheung et al., 2012; Exner and Tschegg, 2012; Skurtveit et al., 2013), which may have had an impact on the analyzed deformation bands. Still, the circumstance that the splay zones enclose unaltered host rock (Figs. 4c,d) highlights the potential of deformation bands to act as baffles to fluid flow.

Apart from the broader meter-scale control on host rock alteration that dominantly occurs in the footwall, the deformation bands exhibit a control at the cm-scale on alteration on both the hanging wall and footwall sides as indicated by the dark red-stained zones along them (Fig. 4d). As seen in the microscopic analysis, the coloration of this zone is caused by the dominant precipitation of Fe-/Ti-oxides and jarosite. The occurrence of these precipitates along biotite flakes or in their close proximity suggests that they form products of its alteration (Bisdom et al., 1982; Morad, 1990; Li et al., 1998). To a minor degree, jarosite and Fe-/Ti-oxides occur outside this zone, where they are mostly confined to parts of mica grains where the flakes have been delaminated. This expansion may have resulted from compaction where the mica grains are mechanically pressed against adjacent grains and subsequently increased the reaction surface for the mica alteration (Figs. 6f,g). An expansion of mica lamellae due to crystal growth in between is less likely as a main driver, since the space

366 between the lamellae is frequently not filled, or only partially filled, with precipitates (Figs.
367 6g,h).

368 Deformation bands are commonly surrounded by a thin envelope, i.e. a 'transition
369 zone', where the degree of compaction is slightly higher than the host rock (e.g., Aydin, 1978;
370 Underhill and Woodcock, 1987; Cavailhes and Rotevatn, 2018). Hence, in this zone, due to
371 the increased compaction, biotite is folded and delaminated to a larger extent providing more
372 reaction surface than in the host rock. Inside the deformation bands, biotite is crushed,
373 however, and Fe-/Ti-oxides and jarosite are nearly absent. This may be rooted in the
374 permeability contrast with the deformation band being low-permeable, while in the
375 surrounding transition zone, the pore space is still large enough to allow for fluid flux
376 providing sufficient reactants for biotite alteration. Capillary effects may also favor fluid
377 migration in the transition zone, rather in the host rock (Sigda and Wilson, 2003; Dimmen et
378 al., 2020). The fact that along the bands of samples G-49 and G-50 the red-stained zone
379 occurs on both sides of the band argues for a similar or the same fluid and a similar fluid
380 circulation habit in the footwall and hanging wall of the bands.

381

382 **5.3 Vein structure**

383 The overall N-NE trend of the veins is oblique to the NW-trending Dombjerg Fault,
384 which may root in the proximity of the outcrop locations to the right-stepping transfer/relay
385 zone between the Dombjerg Fault and the Thomsen Land Fault (Figs. 1b, 2). In such a right-
386 stepping setting, local stress perturbation and clockwise re-orientation of the principal stress
387 axes is common (e.g., Çiftçi and Bozkurt, 2007; Rotevatn and Bastesen, 2012; Mercuri et al.,
388 2020), which may explain the overall trend of the veins. However, the setting is complicated
389 by the circumstance that the majority of the veins formed in the post-rift stage in the
390 Aptian/Albian and it is inferred that the vein ages also reflect the time of fracturing (Salomon

et al., 2020). Activity of the Dombjerg and Thomsen Land faults in the post-rift stage has not been reported. However, the presence of the transfer zone should still cause local stress perturbations and may therefore influence deformation in response to any regional tectonic activity (e.g., Kattenhorn et al., 2000). Nevertheless, as the vein density increases towards the Dombjerg Fault (Kristensen et al., 2016), activity of the fault also in the post-rift stage does seem plausible, albeit this cannot be independently confirmed by our data.

All veins of the hanging wall show at least one generation of syntaxial growth, which argues for a sudden rather than a creeping fracture opening (e.g., Bons et al., 2012). The series of crack-seal events visible in many veins indicate repetitive opening of the veins, albeit, given the width of the crack-seal generations, these latter fracture openings have never exceeded the initial fracture width. In conjunction with the occurrence of slip zones in some of the veins, this suggests that the initial site of fracturing had been preferential zones of weaknesses susceptible for further fracturing, which is a common observation (e.g., Ramsay, 1980; Petit et al., 1999). The low degree of twinning of the vein calcite indicates that the veins have not been subject to significant deformation or high temperatures after their formation (Burkhard, 1993).

5.4 Microcrystalline calcite

The microcrystalline calcite is an intriguing vein infill that differs significantly from the common elongate/blocky calcite crystal generations. From the observations in thin sections of the microcrystalline calcite-hosting veins (Figs. 9, 10), the following interpretations can be drawn:

- The prominent normal gradation in many fill generations (Figs. 10a,b,d,e) indicate that the components were in suspension in a fluid before being deposited (e.g.,

Amy et al., 2006). Normal gradation has also been reported from sand injectites and interpreted to result from settlement in a low-grain concentration fluid (Hubbard et al., 2007; Hurst et al., 2011). Microcrystalline calcite was not found as cement in the sandstone, indicating that this calcite precipitated from the fluid in the fracture. The appearance of microcrystalline calcite also distinguishes these structures from sand injectites, the latter not being associated with mineral precipitation. The circumstance that the clast infill is largely embedded in the microcrystalline calcite (Fig. 10) argues for a calcite precipitation predominantly prior to the settling of clasts.

- The aligned generations of microcrystalline calcite parallel to the wall rock in sample G-9 (Fig. 10a) argue for a repetitive fracture opening with repetitive pulses of microcrystalline calcite precipitation. In sample G-37 (Fig. 10d), such alignment is missing, and generations are solely stacked on top of each other. Combined with the horizontal separation of elongate and microcrystalline calcite in vein G-13 (Fig. 10f), this indicates that the amount of microcrystalline calcite can be heterogeneously distributed within a fracture. A reason for this heterogeneity may be a variable fracture aperture and surface roughness of the fracture walls, which generally influence fluid flow velocities and causes non-linear to turbulent flow and may even create eddies (e.g., Wang et al., 2016; Zou et al., 2015). Subsequently, precipitates and particles that are in suspension may settle when being transported into sections of the fracture where low flow velocities prevail.

Microcrystalline calcite is a rather uncommon calcite texture and has rarely been described before in veins (Eichhubl and Boles, 1998, Bishop and Sumner, 2006; Hendry and Poulsom, 2006; Capezzuoli et al., 2018, as the only examples known to the authors of this contribution). Commonly, calcite preferably grows on nuclei and existing calcite crystals

resulting in the formation of larger crystals (e.g., Bons et al., 2012). We therefore speculate that microcrystalline calcite may have formed in a setting of quick super-saturation that forced a sudden precipitation of calcite from the hosting fluid, preventing an organization of dissolved ions into larger crystals, as similarly proposed for the formation of microcrystalline quartz (Fournier, 1985; Onasch et al., 2010; Shimizu, 2014). A quick super-saturation may be caused by three mechanisms: a sudden pressure drop (e.g., He et al., 1999), a sudden rise of fluid temperature (calcite has a T retrograde solubility; e.g., Plummer and Busenberg, 1982), and fluid mixing (e.g., Tartakovsky et al., 2008).

We regard the influence of temperature as less likely, as we do not identify a heat source that could have caused a sudden local temperature rise. Fluid mixing, which has been considered by Bishop and Sumner (2006), appears plausible in the setting along the Dombjerg Fault, as a fluid in uncemented sediment enclosed by the cementation zone may have a different composition than a fluid outside the cementation zone. Fracturing of cemented layers may connect and mix these fluids causing calcite precipitation within the fracture. This may explain the occurrence of microcrystalline calcite only in fractures. After some time, fluids may reach equilibrium and calcite precipitation continues at a slower rate under normal advective conditions.

Pressure drop and corresponding CO_2 degassing has been proposed as responsible for microcrystalline vein calcite (Eichhubl and Boles, 1998; Bishop and Sumner, 2006; Capezzuoli et al., 2018). Also, fault-induced pore pressure changes are suggested to be responsible for near-fault microcrystalline calcite in clastic sediments (Balsamo et al., 2012). As uncemented porous deposits are susceptible to mechanical compaction (e.g., Paxton et al., 2002), fluid pressure would generally build up in these sediments in response to progressive burial and if enclosed by the low-permeable cemented rock preventing a significant escape of the fluid (e.g., Osborne and Swarbrick, 1997). In addition, organic material degradation,

which is regarded as source of carbon for the calcite cement and veins along the Dombjerg Fault (Salomon et al., 2020), would increase the CO_2 partial pressure (pCO_2) in these enclosed porous compartments (e.g., Schulz and Zabel, 2006). Both the increase of fluid pressure and pCO_2 would act positively on the solubility of calcite (e.g., Stumm and Morgan, 1996; Coto et al., 2012).

If the sealing cemented layer covering the uncemented compartments is breached by a fracture, the overpressured fluid would flow into the fracture and be subject to a sudden fluid pressure and pCO_2 drop within the fracture (Sibson et al., 1988). In addition, if the fracture acts as a narrow pathway that connects two uncemented compartments, fluid pressure should be lower within the fracture than in the compartments above and below the fracture ("Venturi effect"; see e.g., Furbish, 1997; Zhang, 2017). Both mechanisms favor sudden super-saturation within the fracture, leading to quick precipitation of calcite; they may also serve as an explanation for the preferred occurrence of microcrystalline calcite in the fracture and its absence in the pore space of the surrounding host rocks.

Carbon isotopes of vein calcite shed light on the conditions during calcite precipitation. $\delta^{13}C$ of calcite is dependent on the temperature-sensitive carbon isotope fractionation between $CO_{2(g)}$ and calcite (Romanek et al., 1992), which leads to an enrichment of ^{13}C in calcite compared to parent fluid CO_2. In case of a fast pressure drop, CO_2 degassing would result in a kinetic fractionation and further enrichment of ^{13}C in calcite (e.g. Usdowski et al., 1979; Kele et al., 2011).

Knowing the precipitation temperature of calcite, the carbon isotopic composition of parent fluid CO_2 can be calculated using the fractionation equation of Romanek et al. (1992). The formation temperature of a microcrystalline calcite vein was determined as ~40°C (sample G10v1 of Salomon et al. 2020). Using this estimate and an average $\delta^{13}C_{VPDB}$ of -14.8 ‰ for the microcrystalline calcite (Table 2), a $\delta^{13}C_{VPDB}$ value of -22.0 ‰ is calculated for

parent fluid CO_2. In comparison, carbon isotopes of blocky calcite veins that precipitated at similar temperatures of ~36 - 47°C (i.e. samples G-4, G-36v1, G-40, TBK1 of Salomon et al., 2020) yield a range of $\delta^{13}C_{VPDB}$ -23.5 to -19.0 ‰ (average -21.2 ‰). This translates into an average $\delta^{13}C_{VPDB}$ of -28.0 ‰ for fluid CO_2, which is 6.0 ‰ lighter compared to the value of -22.0 ‰ obtained from the microcrystalline calcite generations. A fluid CO_2 $\delta^{13}C_{VPDB}$ value of -28.0 ‰ is in good agreement with the carbon isotopic composition of organic carbon between -31 to -27.5 ‰ measured on mid-Volgian / Ryazanian deposits in the study region (Pauly et al., 2013; Koevoets et al., 2018; Jelby et al., 2020), i.e. the time of deposition of the Lindemans Bugt Formation. This (a) supports the interpretation of Salomon et al. (2020) that CO_2 from the degradation of organic matter was the main carbon source and (b) suggests that the blocky calcite veins formed in near-isotopic equilibrium with fluid CO_2. Further, the significantly higher $\delta^{13}C$ of microcrystalline calcite argues for kinetic isotope fractionation during CO_2 degassing and rapid calcite precipitation.

In summary, for the formation of these veins, we propose a model starting with a tectonic fracture opening (Fig. 11a) indicated by the overall parallel orientation of fractures. Overpressured fluid would inject into the fracture, and the accompanied fluid pressure drop and sudden supersaturation of the fluid in the fracture would force the precipitation of calcite. The energy of the injected fluid would be sufficiently large to carry sediment grains from the uncemented bodies into the fracture. Grains may have also trickled down into the fracture from a potentially overlying uncemented sediment bed or derived from the immediate cemented wall rocks. The latter seems less likely as a significant contributor though, as the fracture walls are rather smooth with cut-off grains, and there is no evidence to support grain fall-out from fracture wall, apart from larger rock fragments. Upon reduction of fluid overpressure, clasts and calcite crystals settle in a normal grading manner (Fig. 11b). Fluid flow within a fracture is often non-linear and may even be turbulent (e.g., Wang et al., 2016;

Zou et al., 2015) giving rise to an unequal deposition of grains, rock fragments and precipitating microcrystalline calcite within the fracture (Figs. 11b,c). The existence of multiple fracture fill generations indicates a cyclicity in their formation. The settling of microcrystalline calcite from suspension may seal the fracture allowing a renewed buildup of fluid pressure in the underlying sediment. Hydraulic (Fig. 11c) or tectonic (Fig. 11d) fracturing would allow the repetitive injection of fluid into the fracture with the corresponding pressure release and microcrystalline calcite precipitation. At moderate fluid pressure and saturation, the formation of blocky calcite would commence in the fracture (Figs. 11e,f).

6. Summary and conclusions

Activity of the Dombjerg Fault and the connected formation of a cementation zone in its proximity (Kristensen et al., 2016; Salomon et al., 2020) has created an environment that showcases, on a microstructural scale, the interaction of sediment diagenesis, tectonic-controlled deformation, and fluid chemistry and flow in clastic rocks along rift-bounded fault systems. By studying the contrasting deformation regimes inside and outside the cementation zone, respectively, we reach the following conclusions regarding the interplay between deformation, fluid flow and diagenesis that followed after the establishment of the fault-proximal cementation zone:

- In the uncemented zones, deformation bands are the common deformation feature, and are characterized by a cataclastic reduction in grain size, which have led to a reduction in porosity and, likely, permeability, within the bands.
- Alteration at and around the deformation bands indicate that the bands acted as partial baffles to fluid flow and resulted in localized host rock alterations, promoting further chemical reduction of porosity.

- In near-impermeable cemented deposits, discrete brittle fractures (veins) are the common deformation features. Microstructuraly, the veins show at least one generation of syntaxial growth, and a series of crack-seal is evident in many veins, indicating repetitive opening and cementation.
- Based on our observations, we suggest the veins comprising microcrystalline calcite formed by rapid precipitation during repetitive fracture opening and injection of fluids. These fluids likely derive from overpressured uncemented deposit compartments that have been enclosed by cemented sediment.

These observations highlight how a fault-controlled calcite cementation zone is able to compartmentalize a syn-rift sedimentary basin into different regimes of fluid flow and deformation. Within fault-proximal cementation zones, fluid flow through pores in the matrix becomes is low to negligible where cementation is pervasive, and fluid flow becomes increasingly dependent on flow through fractures. Outside the zone of fault-proximal pervasive cementation, fluid flow predominantly happens as flow in the matrix porosity (e.g. in the pore space between clastic grains. Understanding this duality in the porosity/fluid flow and deformation regime has important implications for predicting flow patterns, for example in connection with the assessment and planning of potential CO_2 storage, hydrocarbon exploration and production, groundwater aquifers, and geothermal sites (e.g., placement of well sites). It further demonstrates that understanding the interplay between diagenesis, deformation and fluid flow during the evolution of fault-bounded basins is critical, and must be taken into account when evaluating basin histories for a range of applications.

Acknowledgments

Arild Andresen is thanked for advise and logistical support for the field campaign. Michael Joachimski is thanked for discussions and support on the carbon isotope analysis. Constructive reviews by Fabrizio Balsamo and Randolph T. Williams are gratefully acknowledged. Ian Alsop is thanked for editorial handling. The Ministry of Environment and Nature and the Mineral License and Safety Authority of the government of Greenland are thanked for allowing access to the Northeast Greenland National Park for fieldwork conducted under KNNO expedition permit C-18-56 and Scientific Survey License VU-00141. Daniel Koehn and Matteo Demurtas are thanked for helpful discussions. This research was conducted as part of the ARCEx project and has been supported by the Research Council of Norway (grant no. 228107).

References

Amy, L.A., Talling, P.J., Edmonds, V.O., Sumner, E.J., Lesueur, A., 2006. An experimental investigation of sand?mud suspension settling behaviour: implications for bimodal mud contents of submarine flow deposits. Sedimentology 53, 1411–1434. https://doi.org/10.1111/j.1365-3091.2006.00815.x.

Antonellini, M., Aydin, A., 1994. Effect of Faulting on Fluid Flow in Porous Sandstones: Petrophysical Properties. Bulletin 78. https://doi.org/10.1306/BDFF90AA-1718-11D7-8645000102C1865D.

Antonellini, M, Aydin, A., 1995. Effect of Faulting on Fluid Flow in Porous Sandstones: Geometry and Spatial Distribution. AAPG Bulletin 79, 642-671. https://doi.org/10.1306/8D2B1B60-171E-11D7-8645000102C1865D.

Antonellini, M.A., Aydin, A., Pollard, D.D., 1994. Microstructure of deformation bands in porous sandstones at Arches National Park, Utah. Journal of Structural Geology 16, 941–959. https://doi.org/10.1016/0191-8141(94)90077-9.

Aydin, A., 1978. Small Faults Formed as Deformation Bands in Sandstone, in: Rock Friction and Earthquake Prediction. Birkhäuser, Basel, pp. 913–930.

589 Aydin, A., Johnson, A.M., 1983. Analysis of faulting in porous sandstones. Journal of
590 Structural Geology 5, 19–31. https://doi.org/10.1016/0191-8141(83)90004-4.

591 Ballas, G., Fossen, H., Soliva, R., 2015. Factors controlling permeability of cataclastic
592 deformation bands and faults in porous sandstone reservoirs. Journal of Structural
593 Geology 76, 1–21. https://doi.org/10.1016/j.jsg.2015.03.013.

594 Ballas, G., Soliva, R., Sizun, J.-P., Benedicto, A., Cavailhes, T., Raynaud, S., 2012. The
595 importance of the degree of cataclasis in shear bands for fluid flow in porous sandstone,
596 Provence, FranceCataclastic Shear Bands and Fluid Flow in Porous Sandstone. AAPG
597 Bulletin 96, 2167–2186. https://doi.org/10.1306/04051211097.

598 Balsamo, F., Bezerra, F.H.R., Vieira, M.M., Storti, F., 2013. Structural control on the
599 formation of iron-oxide concretions and Liesegang bands in faulted, poorly lithified
600 Cenozoic sandstones of the Paraíba Basin, Brazil. GSA Bulletin 125, 913–931.
601 https://doi.org/10.1130/B30686.1.

602 Balsamo, F., Storti, F., Gröcke, D.R., 2012. Fault-related fluid flow history in shallow marine
603 sediments from carbonate concretions, Crotone basin, south Italy. Journal of the
604 Geological Society 169, 613–626. https://doi.org/10.1144/0016-76492011-109.

605 Baumgartner, L.K., Reid, R.P., Dupraz, C., Decho, A.W., Buckley, D.H., Spear, J.R.,
606 Przekop, K.M., Visscher, P.T., 2006. Sulfate reducing bacteria in microbial mats:
607 Changing paradigms, new discoveries. Sedimentary Geology 185, 131–145.
608 https://doi.org/10.1016/j.sedgeo.2005.12.008.

609 Bellani, S., Brogi, A., Lazzarotto, A., Liotta, D., Ranalli, G., 2004. Heat flow, deep
610 temperatures and extensional structures in the Larderello Geothermal Field (Italy):
611 constraints on geothermal fluid flow. Journal of Volcanology and Geothermal Research
612 132, 15–29. https://doi.org/10.1016/S0377-0273(03)00418-9.

613 Bense, V.F., Gleeson, T., Loveless, S.E., Bour, O., Scibek, J., 2013. Fault zone hydrogeology.
614 Earth-Science Reviews 127, 171–192. https://doi.org/10.1016/j.earscirev.2013.09.008.

615 Bisdom, E.B.A., Stoops, G., Delvigne, J., Curmi, P., Altemuller, H.-J., 1982.
616 Micromorphology of weathering biotite and its secondary products. Pedologie, 225–252.

617 Bishop, J.W., Sumner, D.Y., 2006. Molar tooth structures of the Neoarchean Monteville
618 Formation, Transvaal Supergroup, South Africa. I: Constraints on microcrystalline CaCO3
619 precipitation. Sedimentology 53, 1049–1068. https://doi.org/10.1111/j.1365-
620 3091.2006.00801.x.

621 Bjørlykke, K., 1988. Chapter 2 Sandstone Diagenesis in Relation to Preservation, Destruction
622 and Creation of Porosity, in: Chilingar, G.V., Wolf, K.H. (Eds.), Diagenesis, I, vol. 41.
623 Elsevier, Amsterdam, New York, New York, N.Y., U.S.A, pp. 555–588.

Bons, P.D., Elburg, M.A., Gomez-Rivas, E., 2012. A review of the formation of tectonic veins and their microstructures. Journal of Structural Geology 43, 33–62. https://doi.org/10.1016/j.jsg.2012.07.005.

Burkhard, M., 1993. Calcite twins, their geometry, appearance and significance as stress-strain markers and indicators of tectonic regime: a review. Journal of Structural Geology 15, 351–368. https://doi.org/10.1016/0191-8141(93)90132-t.

Burley, S.D., Worden, R.H. (Eds.), 2003. Sandstone diagenesis: Recent and ancient. Blackwell, [Oxford], 1 livre électronique (e-book).

Capezzuoli, E., Ruggieri, G., Rimondi, V., Brogi, A., Liotta, D., Alçiçek, M.C., Alçiçek, H., Bülbül, A., Gandin, A., Meccheri, M., Shen, C.-C., Baykara, M.O., 2018. Calcite veining and feeding conduits in a hydrothermal system: Insights from a natural section across the Pleistocene Gölemezli travertine depositional system (western Anatolia, Turkey). Sedimentary Geology 364, 180–203. https://doi.org/10.1016/j.sedgeo.2017.12.012.

Cavailhes, T., Rotevatn, A., 2018. Deformation bands in volcaniclastic rocks – Insights from the Shihtiping tuffs, Coastal Range of Taiwan. Journal of Structural Geology 113, 155–175. https://doi.org/10.1016/j.jsg.2018.06.004.

Cheung, C.S.N., Baud, P., Wong, T.- f., 2012. Effect of grain size distribution on the development of compaction localization in porous sandstone. Geophysical Research Letters 39. https://doi.org/10.1029/2012GL053739.

Çiftçi, N.B., Bozkurt, E., 2007. Anomalous stress field and active breaching at relay ramps: a field example from Gediz Graben, SW Turkey. Geological Magazine 144, 687–699. https://doi.org/10.1017/S0016756807003500.

Cook, J.E., Goodwin, L.B., Boutt, D.F., Tobin, H.J., 2015. The effect of systematic diagenetic changes on the mechanical behavior of a quartz-cemented sandstone. Bulletin 80, D145-D160. https://doi.org/10.1190/geo2014-0026.1.

Coto, B., Martos, C., Peña, J.L., Rodríguez, R., Pastor, G., 2012. Effects in the solubility of CaCO3: Experimental study and model description. Fluid Phase Equilibria 324, 1–7. https://doi.org/10.1016/j.fluid.2012.03.020.

Del Sole, L., Antonellini, M., Soliva, R., Ballas, G., Balsamo, F., Viola, G., 2020. Structural control on fluid flow and shallow diagenesis: insights from calcite cementation along deformation bands in porous sandstones. Solid Earth 11, 2169–2195. https://doi.org/10.5194/se-11-2169-2020.

Dimmen, V., Rotevatn, A., Nixon, C.W., 2020. The Relationship between Fluid Flow, Structures, and Depositional Architecture in Sedimentary Rocks: An Example-Based Overview. Geofluids 2020. https://doi.org/10.1155/2020/3506743.

Dyke, C.G., Dobereiner, L., 1991. Evaluating the strength and deformability of sandstones. Quarterly Journal of Engineering Geology and Hydrogeology 24, 123–134. https://doi.org/10.1144/GSL.QJEG.1991.024.01.13.

Eichhubl, P., Boles, J.R., 1998. Vein formation in relation to burial diagenesis in the Miocene Monterey Formation, Arroyo Burro beach, Santa Barbara, California. Pacific Section SEPM Special Publication, 15–36.

Eichhubl, P., Boles, J.R., 2000. Focused fluid flow along faults in the Monterey Formation, coastal California. Geological Society of America Bulletin 112, 1667–1679. https://doi.org/10.1130/0016-7606(2000)112<1667:FFFAFI>2.0.CO;2.

Exner, U., Tschegg, C., 2012. Preferential cataclastic grain size reduction of feldspar in deformation bands in poorly consolidated arkosic sands. Journal of Structural Geology 43, 63–72. https://doi.org/10.1016/j.jsg.2012.08.005.

Fisher, Q.J., Casey, M., Harris, S.D., Knipe, R.J., 2003. Fluid-flow properties of faults in sandstone: The importance of temperature history. Geology 31, 965. https://doi.org/10.1130/G19823.1.

Fossen, H., Bale, A., 2007. Deformation bands and their influence on fluid flow. AAPG Bulletin 91, 1685–1700. https://doi.org/10.1306/07300706146.

Fossen, H., Soliva, R., Ballas, G., Trzaskos, B., Cavalcante, C., Schultz, R.A., 2018. A review of deformation bands in reservoir sandstones: geometries, mechanisms and distribution. Geological Society, London, Special Publications 459, 9–33. https://doi.org/10.1144/SP459.4.

Fournier, R.O., 1985. The behavior of silica in hydrothermal solutions. Review in Economic Geology 2, 45–60.

Furbish, D.J., 1997. Fluid Physics in Geology: An Introduction to Fluid Motions on Earth's Surface and within Its Crust. Oxford University Press.

Gawthorpe, R.L., Leeder, M.R., 2000. Tectono-sedimentary evolution of active extensional basins. Basin Research 12, 195–218. https://doi.org/10.1046/j.1365-2117.2000.00121.x.

Gibson, R.G., 1998. Physical character and fluid-flow properties of sandstone-derived fault zones. Geological Society, London, Special Publications 127, 83–97. https://doi.org/10.1144/GSL.SP.1998.127.01.07.

He, S., Kan, A.T., Tomson, M.B., 1999. Inhibition of calcium carbonate precipitation in NaCl brines from 25 to 90°C. Applied Geochemistry 14, 17–25. https://doi.org/10.1016/S0883-2927(98)00033-X.

Hendry, J.P., Poulsom, A.J., 2006. Sandstone-hosted concretions record evidence for syn-lithification seismicity, cavitation processes, and Palaeocene rapid burial of Lower

694 Cretaceous deep-marine sandstones (Outer Moray Firth, UK North Sea). Journal of the
695 Geological Society 163, 447–460. https://doi.org/10.1144/0016-764905-033.

696 Henriksen, N., 2003: Caledonian Orogen East Greenland 70–82∘ N, Geological map
697 1:100 000, Tech. rep., GEUS, Copenhagen, Greenland, p. 1.

698 Henstra, G.A., Grundvåg, S.-A., Johannessen, E.P., Kristensen, T.B., Midtkandal, I., Nystuen,
699 J.P., Rotevatn, A., Surlyk, F., Sæther, T., Windelstad, J., 2016. Depositional processes and
700 stratigraphic architecture within a coarse-grained rift-margin turbidite system: The
701 Wollaston Forland Group, east Greenland. Marine and Petroleum Geology 76, 187–209.
702 https://doi.org/10.1016/j.marpetgeo.2016.05.018.

703 Houseknecht, D.W., 1987. Assessing the Relative Importance of Compaction Processes and
704 Cementation to Reduction of Porosity in Sandstones. AAPG Bulletin 71.
705 https://doi.org/10.1306/9488787F-1704-11D7-8645000102C1865D.

706 Hubbard, S.M., Romans, B.W., Graham, S.A., 2007. An Outcrop Example of Large-scale
707 Conglomeratic Intrusions Sourced from Deep-water Channel Deposits, Cerro Toro
708 Formation, Magallanes Basin, Southern Chile, in: Hurst, A., Cartwright, J. (Eds.), Sand
709 injectites: implications for hydrocarbon exploration and production. The American
710 Association of Petroleum Geologists, Tulsa, Okla, pp. 199–207.

711 Hurst, A., Scott, A., Vigorito, M., 2011. Physical characteristics of sand injectites. Earth-
712 Science Reviews 106, 215–246. https://doi.org/10.1016/j.earscirev.2011.02.004.

713 Jelby, M.E., Śliwińska, K.K., Koevoets, M.J., Alsen, P., Vickers, M.L., Olaussen, S.,
714 Stemmerik, L., 2020. Arctic reappraisal of global carbon-cycle dynamics across the
715 Jurassic–Cretaceous boundary and Valanginian Weissert Event. Palaeogeography,
716 Palaeoclimatology, Palaeoecology 555, 109847.
717 https://doi.org/10.1016/j.palaeo.2020.109847.

718 Kattenhorn, S.A., Aydin, A., Pollard, D.D., 2000. Joints at high angles to normal fault strike:
719 an explanation using 3-D numerical models of fault-perturbed stress fields. Journal of
720 Structural Geology 22, 1–23. https://doi.org/10.1016/s0191-8141(99)00130-3.

721 Kele, S., Özkul, M., Fórizs, I., Gökgöz, A., Baykara, M.O., Alçiçek, M.C., Németh, T., 2011.
722 Stable isotope geochemical study of Pamukkale travertines: New evidences of low-
723 temperature non-equilibrium calcite-water fractionation. Sedimentary Geology 238, 191–
724 212. https://doi.org/10.1016/j.sedgeo.2011.04.015.

725 Knipe, R., 1993. The influence of fault zone processes and diagenesis on fluid flow. In:
726 Horbury, A.D., Robinson, A.G. (Eds.), Diagenesis and Basin Development. Studies in
727 Geology 36. American Association of Petroleum Geologists, pp. 135-154.

728 Koevoets, M.J., Hammer, Ø., Olaussen, S., Senger, K., Smelror, M., 2018. Integrating
729 subsurface and outcrop data of the Middle Jurassic to Lower Cretaceous Agardhfjellet

730 Formation in central Spitsbergen. Norsk Geologisk Tidsskrift 98, 219-252.
731 https://doi.org/10.17850/njg98-4-01.

732 Kristensen, T.B., Rotevatn, A., Peacock, D.C.P., Henstra, G.A., Midtkandal, I., Grundvåg, S.-
733 A., 2016. Structure and flow properties of syn-rift border faults: The interplay between
734 fault damage and fault-related chemical alteration (Dombjerg Fault, Wollaston Forland,
735 NE Greenland). Journal of Structural Geology 92, 99–115.
736 https://doi.org/10.1016/j.jsg.2016.09.012.

737 Larsen, L.M., Watt, W.S., 1985. Episodic volcanism during break-up of the North Atlantic:
738 evidence from the East Greenland plateau basalts. Earth and Planetary Science Letters 73,
739 105–116. https://doi.org/10.1016/0012-821X(85)90038-X.

740 Laubach, S.E., Eichhubl, P., Hilgers, C., Lander, R.H., 2010. Structural diagenesis. Journal of
741 Structural Geology 32, 1866–1872. https://doi.org/10.1016/j.jsg.2010.10.001.

742 Li, G., Peacor, D.R., Essene, E.J., 1998. The Formation of Sulfides During Alteration of
743 Biotite to Chlorite-Corrensite. Clays Clay Miner. 46, 649–657.
744 https://doi.org/10.1346/CCMN.1998.0460605.

745 Lundegard, P.D., 1992. Sandstone porosity loss; a "big picture" view of the importance of
746 compaction. Journal of Sedimentary Research 62, 250–260.
747 https://doi.org/10.1306/D42678D4-2B26-11D7-8648000102C1865D.

748 Mandl, G., Jong, L.N.J., Maltha, A., 1977. Shear zones in granular material. Rock Mechanics
749 9, 95–144. https://doi.org/10.1007/bf01237876.

750 Menéndez, B., Zhu, W., Wong, T.-F., 1996. Micromechanics of brittle faulting and cataclastic
751 flow in Berea sandstone. Journal of Structural Geology 18, 1–16.
752 https://doi.org/10.1016/0191-8141(95)00076-P.

753 Mercuri, M., McCaffrey, K.J.W., Smeraglia, L., Mazzanti, P., Collettini, C., Carminati, E.,
754 2020. Complex geometry and kinematics of subsidiary faults within a carbonate-hosted
755 relay ramp. Journal of Structural Geology 130, 103915.
756 https://doi.org/10.1016/j.jsg.2019.103915.

757 Morad, S., 1990. Mica Alteration Reactions in Jurassic Reservoir Sandstones from the
758 Haltenbanken Area, Offshore Norway. Clays Clay Miner. 38, 584–590.
759 https://doi.org/10.1346/CCMN.1990.0380603.

760 Onasch, C.M., Farver, J.R., Dunne, W.M., 2010. The role of dilation and cementation in the
761 formation of cataclasite in low temperature deformation of well cemented quartz-rich
762 rocks. Journal of Structural Geology 32, 1912–1922.
763 https://doi.org/10.1016/j.jsg.2010.04.013.

764 Osborne, M.J., Swarbrick, R.E., 1997. Mechanisms for Generating Overpressure in
765 Sedimentary Basins: A Reevaluation. AAPG Bulletin 81, 1023-1041.
766 https://doi.org/10.1306/522B49C9-1727-11D7-8645000102C1865D.

767 Pauly, S., Mutterlose, J., Alsen, P., 2013. Depositional environments of Lower Cretaceous
768 (Ryazanian–Barremian) sediments from Wollaston Forland and Kuhn Ø, North-East
769 Greenland. Bulletin of the Geological Society of Denmark, 19–36.

770 Paxton, S.T., Szabo, J.O., Ajdukiewicz, J.M., Klimentidis, R.E., 2002. Construction of an
771 Intergranular Volume Compaction Curve for Evaluating and Predicting Compaction and
772 Porosity Loss in Rigid-Grain Sandstone Reservoirs. AAPG Bulletin 86, 2047–2067.
773 https://doi.org/10.1306/61EEDDFA-173E-11D7-8645000102C1865D.

774 Petit, J.-P., Wibberley, C.A.J., Ruiz, G., 1999. `Crack–seal', slip: a new fault valve
775 mechanism? Journal of Structural Geology 21, 1199–1207. https://doi.org/10.1016/s0191-
776 8141(99)00038-3.

777 Philit, S., Soliva, R., Ballas, G., Chemenda, A., Castilla, R., 2019. Fault surface development
778 and fault rock juxtaposition along deformation band clusters in porous sandstones series.
779 AAPG Bulletin 103, 2731–2756. https://doi.org/10.1306/01211917256.

780 Phillips, O.M., 2009. Geological Fluid Dynamics. Cambridge University Press, Cambridge.

781 Pittman, E.D., 1981. Effect of Fault-Related Granulation on Porosity and Permeability of
782 Quartz Sandstones, Simpson Group (Ordovician), Oklahoma. AAPG Bulletin 65, 2381-
783 2387. https://doi.org/10.1306/03B5999F-16D1-11D7-8645000102C1865D.

784 Pizzati, M., Balsamo, F., Storti, F., Iacumin, P., 2020. Physical and chemical strain-hardening
785 during faulting in poorly lithified sandstone: The role of kinematic stress field and
786 selective cementation. Geological Society of America Bulletin 132, 1183–1200.
787 https://doi.org/10.1130/B35296.1.

788 Prosser, S., 1993. Rift-related linked depositional systems and their seismic expression.
789 Geological Society, London, Special Publications 71, 35–66.
790 https://doi.org/10.1144/GSL.SP.1993.071.01.03.

791 Ramsay, J.G., 1980. The crack–seal mechanism of rock deformation. Nature 284, 135–139.
792 https://doi.org/10.1038/284135a0.

793 Rawling, G.C., Goodwin, L.B., 2003. Cataclasis and particulate flow in faulted, poorly
794 lithified sediments. Journal of Structural Geology 25, 317–331.
795 https://doi.org/10.1016/S0191-8141(02)00041-X.

796 Romanek, C.S., Grossman, E.L., Morse, J.W., 1992. Carbon isotopic fractionation in
797 synthetic aragonite and calcite: Effects of temperature and precipitation rate. Geochimica
798 et Cosmochimica Acta 56, 419–430. https://doi.org/10.1016/0016-7037(92)90142-6.

Rotevatn, A., Tveranger, J., Howell, J.A., Fossen, H., 2009. Dynamic investigation of the effect of a relay ramp on simulated fluid flow: geocellular modelling of the Delicate Arch Ramp, Utah. Petroleum Geoscience 15, 45–58. https://doi.org/10.1144/1354-079309-779.

Rotevatn, A., Bastesen, E., 2014. Fault linkage and damage zone architecture in tight carbonate rocks in the Suez Rift (Egypt): implications for permeability structure along segmented normal faults. Geological Society, London, Special Publications 374, 79–95. https://doi.org/10.1144/SP374.12.

Rotevatn, A., Kristensen, T.B., Ksienzyk, A.K., Wemmer, K., Henstra, G.A., Midtkandal, I., Grundvåg, S.-A., Andresen, A., 2018. Structural Inheritance and Rapid Rift-Length Establishment in a Multiphase Rift: The East Greenland Rift System and its Caledonian Orogenic Ancestry. Tectonics 37, 1858–1875. https://doi.org/10.1029/2018TC005018.

Salomon, E., Rotevatn, A., Kristensen, T.B., Grundvåg, S.-A., Henstra, G.A., Meckler, A.N., Albert, R., Gerdes, A., 2020. Fault-controlled fluid circulation and diagenesis along basin-bounding fault systems in rifts - insights from the East Greenland rift system. Solid Earth 11, 1987–2013. https://doi.org/10.5194/se-11-1987-2020.

Schulz, H.D., Zabel, M. (Eds.), 2006. Marine Geochemistry. Springer-Verlag, Berlin/Heidelberg.

Shimizu, T., 2014. Reinterpretation of Quartz Textures in Terms of Hydrothermal Fluid Evolution at the Koryu Au-Ag Deposit, Japan. Economic Geology 109, 2051–2065. https://doi.org/10.2113/econgeo.109.7.2051.

Sibson, R.H., Robert, F., Poulsen, K.H., 1988. High-angle reverse faults, fluid-pressure cycling, and mesothermal gold-quartz deposits. Geology 16, 551–555. https://doi.org/10.1130/0091-7613(1988)016<0551:HARFFP>2.3.CO;2.

Sigda, J.M., Wilson, J.L., 2003. Are faults preferential flow paths through semiarid and arid vadose zones? Water Resources Research 39. https://doi.org/10.1029/2002WR001406.

Skurtveit, E., Torabi, A., Gabrielsen, R.H., Zoback, M.D., 2013. Experimental investigation of deformation mechanisms during shear-enhanced compaction in poorly lithified sandstone and sand. J. Geophys. Res. Solid Earth 118, 4083–4100. https://doi.org/10.1002/jgrb.50342.

Stemmerik, L., Vigran, J.O., Piasecki, S., 1991. Dating of late Paleozoic rifting events in the North Atlantic: New biostratigraphic data from the uppermost Devonian and Carboniferous of East Greenland. Geol 19, 218. https://doi.org/10.1130/0091-7613(1991)019<0218:DOLPRE>2.3.CO;2.

Stumm, W., Morgan, J.J., 1996. Aquatic chemistry: Chemical equilibria and rates in natural waters. John Wiley & Sons Inc, New York, 1022 pp.

Surlyk, F., 1984. Fan-Delta to Submarine Fan Conglomerates of the Volgian-Valanginian Wollaston Forland Group, East Greenland. Canadian Society of Petroleum Geology, 359–382.

Surlyk, F., 1990. Timing, style and sedimentary evolution of Late Palaeozoic-Mesozoic extensional basins of East Greenland. Geological Society, London, Special Publications 55, 107–125. https://doi.org/10.1144/GSL.SP.1990.055.01.05.

Surlyk, F., 2003. The Jurassic of Denmark and Greenland: The Jurassic of East Greenland: a sedimentary record of thermal subsidence, onset and culmination of rifting. Geological Survey of Denmark and Greenland Bulletin, 1, 659–722

Surlyk, F., Korstgård, J., 2013. Crestal unconformities on an exposed Jurassic tilted fault block, Wollaston Forland, East Greenland as an analogue for buried hydrocarbon traps. Marine and Petroleum Geology 44, 82–95. https://doi.org/10.1016/j.marpetgeo.2013.03.009.

Tartakovsky, A.M., Redden, G., P. C. Lichtner, P. C., T. D. Scheibe, T. D., Meakin, P., 2008. Mixing- induced precipitation: Experimental study and multiscale numerical analysis. Water Resources Research 44. https://doi.org/10.1029/2006WR005725.

Taylor, T.R., Giles, M.R., Hathon, L.A., Diggs, T.N., Braunsdorf, N.R., Birbiglia, G.V., Kittridge, M.G., Macaulay, C.I., Espejo, I.S., 2010. Sandstone diagenesis and reservoir quality prediction: Models, myths, and reality. AAPG Bulletin 94, 1093–1132. https://doi.org/10.1306/04211009123.

Torabi, A., Fossen, H., 2009. Spatial variation of microstructure and petrophysical properties along deformation bands in reservoir sandstones. AAPG Bulletin 93, 919–938. https://doi.org/10.1306/03270908161.

Torabi, A., Fossen, H., Braathen, A., 2013. Insight into petrophysical properties of deformed sandstone reservoirs. AAPG Bulletin 97, 619–637. https://doi.org/10.1306/10031212040.

Townend, J., Sutherland, R., Toy, V.G., Doan, M.-L., Célérier, B., Massiot, C., Coussens, J., Jeppson, T., Janku-Capova, L., Remaud, L., Upton, P., Schmitt, D.R., Pezard, P., Williams, J., Allen, M.J., Baratin, L.-M., Barth, N., Becroft, L., Boese, C.M., Boulton, C., Broderick, N., Carpenter, B., Chamberlain, C.J., Cooper, A., Coutts, A., Cox, S.C., Craw, L., Eccles, J.D., Faulkner, D., Grieve, J., Grochowski, J., Gulley, A., Hartog, A., Henry, G., Howarth, J., Jacobs, K., Kato, N., Keys, S., Kirilova, M., Kometani, Y., Langridge, R., Lin, W., Little, T., Lukacs, A., Mallyon, D., Mariani, E., Mathewson, L., Melosh, B., Menzies, C., Moore, J., Morales, L., Mori, H., Niemeijer, A., Nishikawa, O., Nitsch, O., Paris, J., Prior, D.J., Sauer, K., Savage, M.K., Schleicher, A., Shigematsu, N., Taylor-Offord, S., Teagle, D., Tobin, H., Valdez, R., Weaver, K., Wiersberg, T., Zimmer, M., 2017. Petrophysical, Geochemical, and Hydrological Evidence for Extensive Fracture-Mediated Fluid and Heat Transport in the Alpine Fault's Hanging-Wall Damage Zone. Geochem. Geophys. Geosyst. 18, 4709–4732. https://doi.org/10.1002/2017GC007202.

872 Underhill, J.R., Woodcock, N.H., 1987. Faulting mechanisms in high-porosity sandstones;
873 New Red Sandstone, Arran, Scotland. Geological Society, London, Special Publications
874 29, 91–105. https://doi.org/10.1144/GSL.SP.1987.029.01.09.

875 Usdowski, E., Hoefs, J., Menschel, G., 1979. Relationship between13C and18O fractionation
876 and changes in major element composition in a recent calcite-depositing spring — A
877 model of chemical variations with inorganic CaCO3 precipitation. Earth and Planetary
878 Science Letters 42, 267–276. https://doi.org/10.1016/0012-821X(79)90034-7.

879 Vanneste, M., Guidard, S., Mienert, J., 2005. Bottom-simulating reflections and geothermal
880 gradients across the western Svalbard margin. Terra Nova 17, 510–516.
881 https://doi.org/10.1111/j.1365-3121.2005.00643.x.

882 Wang, M., Chen, Y.-F., Ma, G.-W., Zhou, J.-Q., Zhou, C.-B., 2016. Influence of surface
883 roughness on nonlinear flow behaviors in 3D self-affine rough fractures: Lattice
884 Boltzmann simulations. Advances in Water Resources 96, 373–388.
885 https://doi.org/10.1016/j.advwatres.2016.08.006.

886 Williams, R.T., Goodwin, L.B., Mozley, P.S., 2017. Diagenetic controls on the evolution of
887 fault-zone architecture and permeability structure: Implications for episodicity of fault-
888 zone fluid transport in extensional basins. Geological Society of America Bulletin 129,
889 464–478. https://doi.org/10.1130/B31443.1.

890 Worden, R.H., Burley, S.D., 2003. Sandstone Diagenesis: The Evolution of Sand to Stone, in:
891 Burley, S.D., Worden, R.H. (Eds.), Sandstone diagenesis: Recent and ancient. Blackwell,
892 [Oxford], pp. 1–44.

893 Zhang, J.X., 2017. Analysis on the effect of venturi tube structural parameters on fluid flow.
894 AIP Advances 7, 65315. https://doi.org/10.1063/1.4991441.

895 Zou, L., Jing, L., Cvetkovic, V., 2015. Roughness decomposition and nonlinear fluid flow in a
896 single rock fracture. International Journal of Rock Mechanics and Mining Sciences 75,
897 102–118. https://doi.org/10.1016/j.ijrmms.2015.01.016.

898

899 **Figure Captions**

900 Figure 1: (a) Regional geological map of NE Greenland with right-stepping rift
901 boundary fault system separating Devonian-Jurassic sedimentary basins from Caledonian
902 basement. (b) Geological map of the Wollaston Forland and its surrounding. (c) Schematic
903 geological cross section of the Wollaston Forland Basin (see (b) for location). Modified after

Rotevatn et al. (2018), based on Surlyk et al. (1993), Surlyk (2003), Henriksen (2003), Surlyk and Korstgård (2013), and Henstra et al. (2016).

Figure 2: Geological map of study area with locations of outcrops and samples analyzed in this study. Inset of stereographic plot shows orientation of calcite veins / deformation bands in the respective outcrops. Sample coordinates provided in supplementary table S1. See Fig. 1b for location. Base satellite image from Google Earth / Digital Globe.

Figure 3: Field photos illustrating characteristics of veins and contact of cemented and uncemented sediments. (a,b) calcite cementation form lobes and appears to partially enclose uncemented sediments; (c) single sediment layers and lenses (light yellowish color) remain devoid of calcite cement in otherwise dominant calcite-cemented strata.

Figure 4: Field photos of deformation bands with orientation and sample position (where available). (a) deformation band offsetting a layer of organic material by ~3 cm normally (apparent reverse displacement is due to cutting effect; location 20). (b) deformation band with no visible offset (location 22). (c) deformation band with ~5 cm normal displacement and exhibiting a splay zone enclosing a section of unaltered host rock; note the preferred reddish alteration of the footwall (location 23). (d) deformation band splay enclosing unaltered host rock; note dark reddish rim along band in the otherwise yellowish host rock (location 23); (e) deformation band showcasing dominant footwall alteration, while hanging wall rock remains unaltered. (f) deformation band cluster that has merged to form a mature fault with an offset >5 m (i.e. larger than exposed vertical section). Note that structures in (e) and (f) are taken ~20 m apart from each other and derive from the same fault (location 26).

Figure 5: Thin section photos of deformation bands. (a,b) samples G-48 and G-49 comprise deformation bands with low degree of cataclasis and subtle boundary to wall rock.

(c,d) sample G-50 with deformation band showing a distinct boundary to the wall rock indicated by the brownish coloration of the latter; (e,f) sample G-57 exhibiting an array of three deformation bands; (g,h) sample G-60, deriving from the core of a cataclastic zone (figure 6f) showing intense grain fracturing and cataclasis in the whole thin section. Images a,c,e,g are taken in polarized incident ring light; d,h in plane-polarized light; f in backscattered electron. Large pores in all images are due to grain plucking during thin section preparation. For locations of samples in the outcrop see figure 4.

Figure 6: Thin section photos of deformation band and wall rock illustrating the degree of biotite alteration (a-g of sample G-50; h, i of sample G-57) in plane polarized light and backscatter electron imaging in and along the deformation band. (b,c) unaltered and intensively deformed biotite within deformation band; (d,e) altered and deformed and broken biotite lamellae with large quantity of Fe-oxides in red-stained zone; (f,g) slightly deformed biotite with alteration and oxide-precipitation restricted to delaminated part of biotite grain in wall rock; (h,i) intense oxide and pyrite precipitation within and near biotite grains in sample G-57 (EDX spectra and element maps in supplements S2).

Figure 7: Thin section photos of deformation bands (sample G-50, G-57) and host rock (sample G-58) with respective porosity values. Notice the porosity reduction from host rock to bands resulting from the cataclastic grain crushing. Porosity reduction also occurs along the bands, due to preferential precipitation of Fe- / Ti- oxides and pyrite (sample G-50). Sample G-58 is taken ~20 cm away from sample G-57 and has a porosity slightly higher than the host rock of G-57. This is in agreement with field appearance with a decrease in red staining away from the cluster of deformation bands. Porosity derived from 2-D image analysis of backscatter electron images (inset overlays in images).

Figure 8: Field photos illustrating the characteristics of veins cutting through cemented deposits. (a) surface of a vein fill consisting of blocky calcite; (b) vein fill consisting of

multiple generations of microcrystalline calcite (location of sample G-9 thin section marked with white frame); (c) calcite vein with a thin rim of microcystalline calcite (sample G-10 derives from this vein, though exact location not in picture); (d) vein consisting of a microcrystalline calcite rim and an infill of microcrystalline calcite and sediment grains (sample G-13 derives from this vein, though exact location not in picture); (e) microcrystalline calcite infill succeeded by elongate calcite growth in upper part of vein (location of sample G-37 thin section marked with white frame). See figure 2 for location of photos.

Figure 9: Thin section photos of calcite veins. (a,b) vein with growth generations that are distinguishable through the degree of dust inclusions; (c,d) vein exhibiting growth zonations with the inclusion of Fe-oxide precipitates; (e,f) vein exhibiting crack-seal texture with inclusion bands; light brownish material is microcystalline calcite (see chapter 4.2 and figure 5 for detailed explanations); (g,h) vein comprising multiple fault slip zones. All images taken in polarized incident ring light.

Figure 10: Thin section photos of three vein samples hosting microcystalline calcite (MC; light brownish mass in cross-polarized light) infill. (a-c) vertical face of sample G-9 shows an array of vein fill generations parallel to the wall rock. Within the generations a repeated gradation of upward fining infill is present. (d, e) vertical face of sample G-37 exhibits multiple generations of upward-fining vein fill, that are succeeded by elongate calcite crystal growth. (f) the horizontal face of sample G-13 shows a transition of vein fill from elongate calcite crystals to MC hosting lithic fragments. Main characteristics in thin sections are pointed out with numbers.

Figure 11: Conceptual model for the formation of microcrystalline calcite infill found in number of veins cutting through cemented sandstone within the cementation zone along the Dombjerg Fault. The inferred main driver for the formation is initial calcite-saturated

overpressured fluid in uncemented sandstone whose injection into a forming fracture is accompanied by sudden fluid pressure drop. This results in an instant super-saturation with respect to calcite and forces its quick precipitation.

Table Captions

Table 1: Porosity data of deformation band samples derived from BSE image analysis (cf. fig. 7).

Table 2: Carbon isotope values of microcrystalline vein generations.

Highlights:

- Fault-controlled fluid flow leads to localized near-fault calcite cementation
- Fault-related cementation compartmentalizes basin into separate deformation and flow regimes
- Non-cemented clastic rock susceptible to deformation band formation and local fluid baffling
- Cemented rock seals uncemented bodies and leads to fluid overpressure released during fracturing
- Study showcases importance of localized cementation for fault-bounded subsurface reservoirs

Author statement

All authors conducted the field data collection, rock sampling, data evaluation, manuscript reviewing and editing. ES handled the analytical data collection and writing of initial manuscript draft.

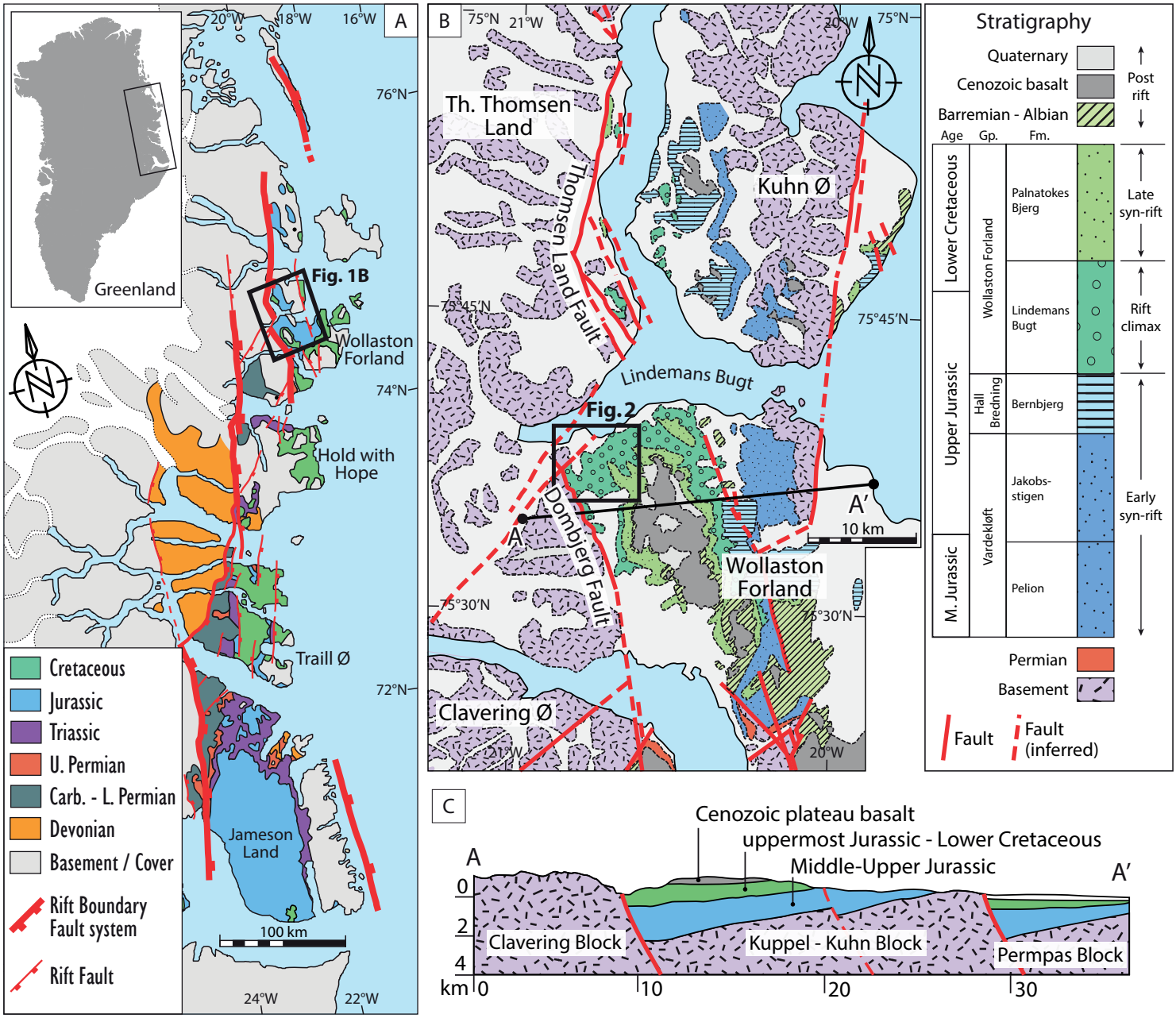

Figure 1. (a) Regional geological map of NE Greenland with right-stepping rift boundary fault system separating Devonian-Jurassic sedimentary basins from Caledonian basement. (b) Geological map of the Wollaston Forland and its surrounding. (c) Geological cross section of the Wollaston Forland Basin (see (b) for location). Modified after Rotevatn et al. (2018), based on Surlyk et al. (1993), Surlyk (2003), Henriksen (2003), Surlyk and Korstgård (2013), and Henstra et al. (2016).

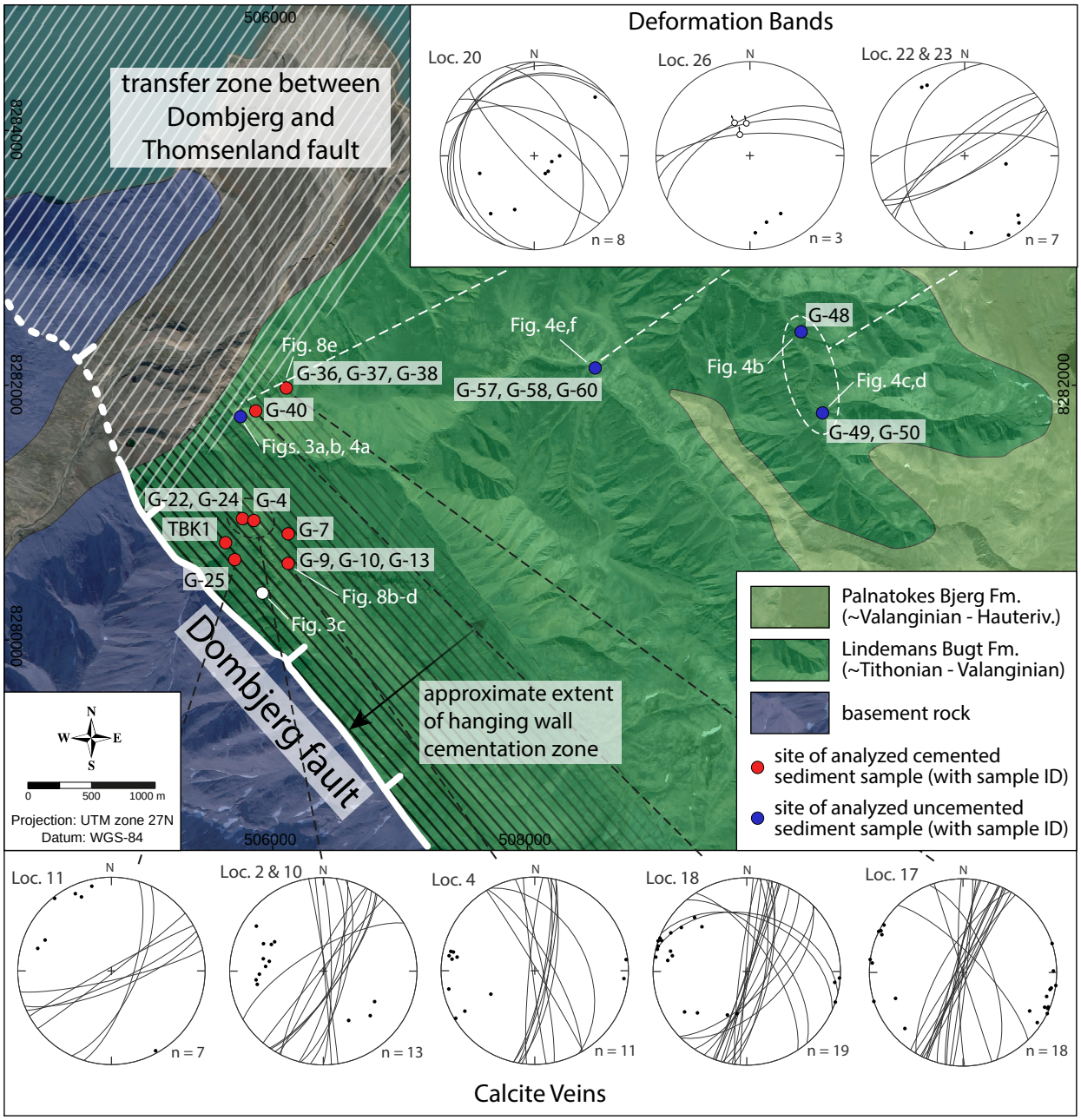

Fig. 2: Geological map of study area with locations of outcrops and samples analyzed in this study. Inset of stereographic plot shows orientation of calcite veins / deformation bands in the respective outcrops. Sample coordinates provided in supplementary table S1. See Fig. 1b for location. Base satellite image from Google Earth / Digital Globe.

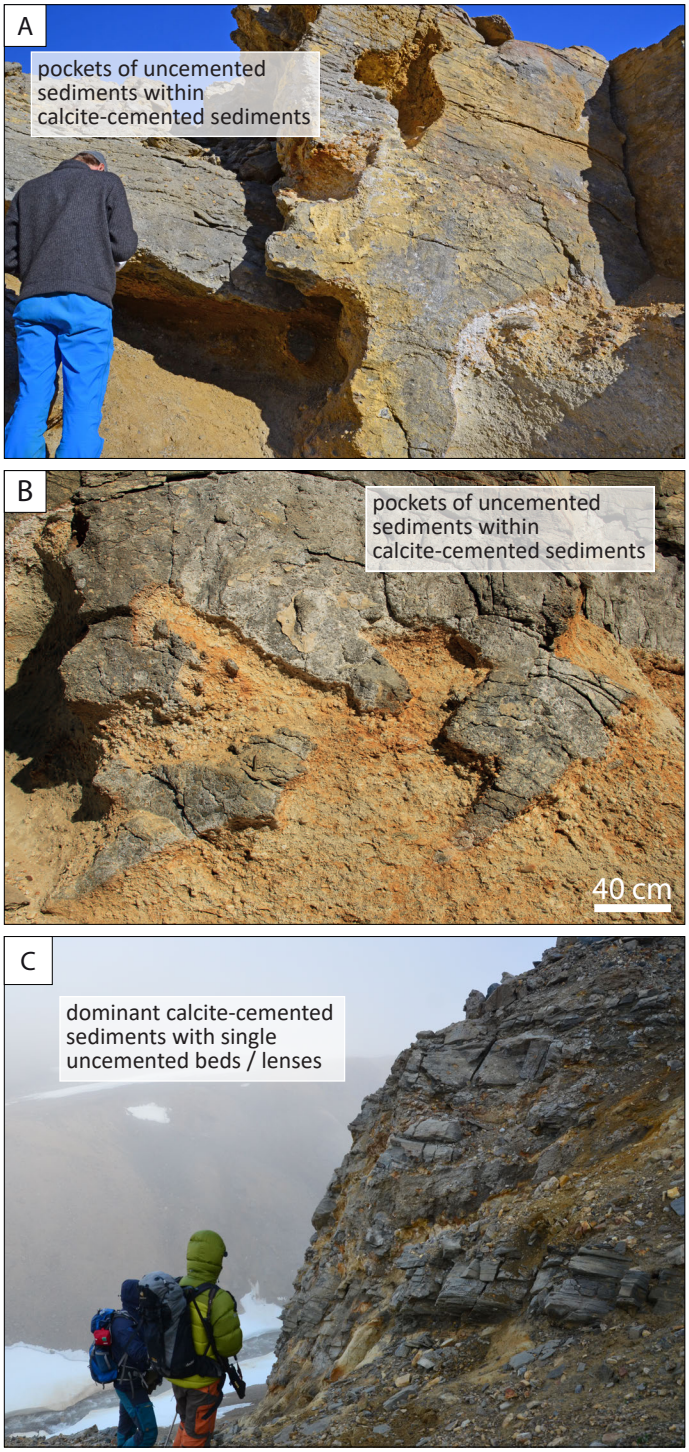

Figure 3: Field photos illustrating characteristics of the contact of cemented and uncemented sediments. (a,b) calcite cementation form lobes and appears to partially enclose uncemented sediments; (c) single sediment layers and lenses (light yellowish color) remain devoid of calcite cement in otherwise dominant calcite-cemented strata.

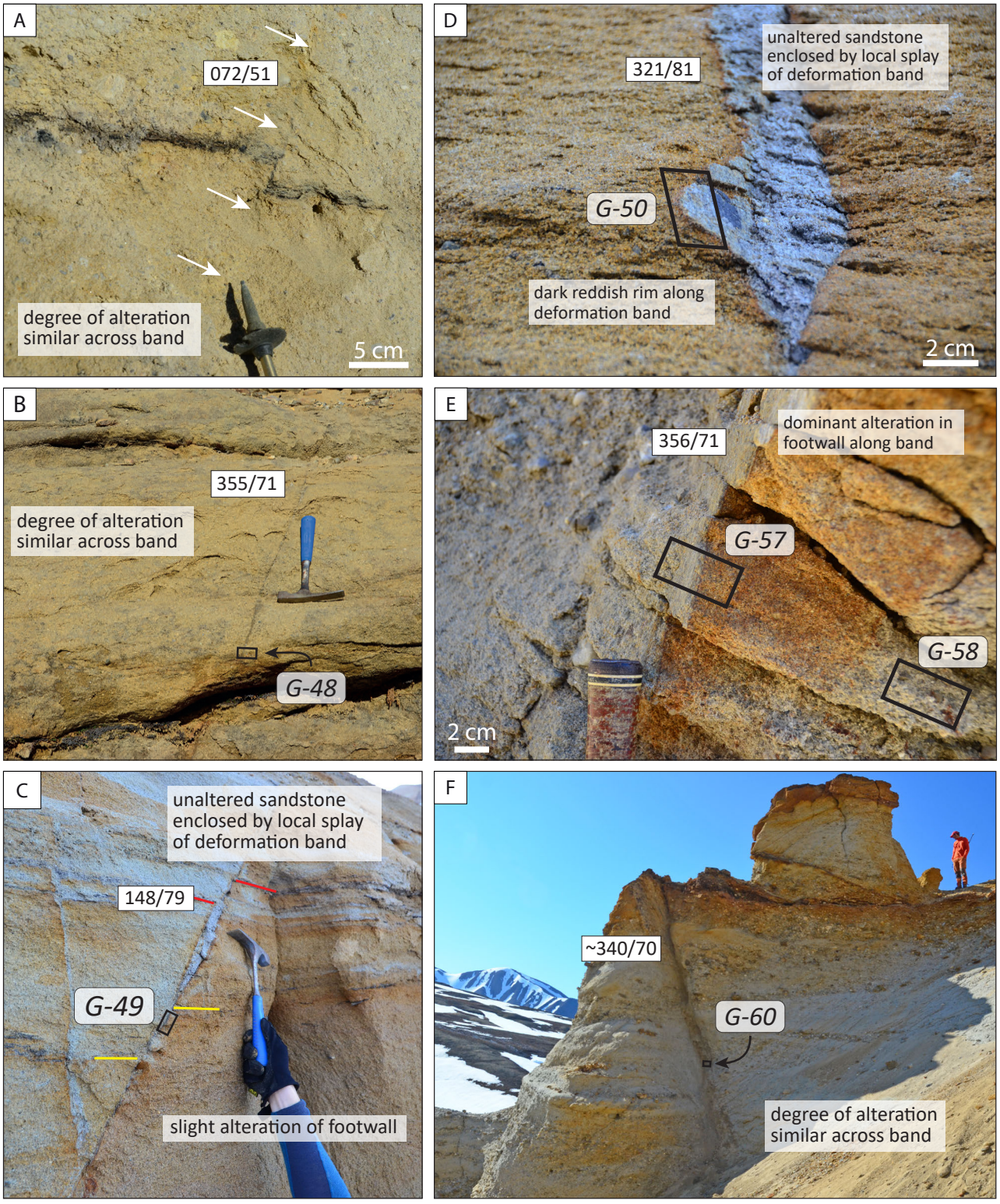

Figure 4: Field photos of deformation bands with orientation and sample position (where available). (a) deformation band offsetting a layer of organic material by ~3 cm normally (apparent reverse displacement is due to cutting effect; location 20). (b) deformation band with no visible offset (location 22). (c) deformation band with ~5 cm normal displacement and exhibiting a splay zone enclosing a section of unaltered host rock; note the preferred reddish alteration of the footwall (location 23). (d) deformation band splay enclosing unaltered host rock; note dark reddish rim along band in the otherwise yellowish host rock (location 23); (e) deformation band showcasing dominant footwall alteration, while hanging wall rock remains unaltered. (f) deformation band cluster that has merged to form a mature fault with an offset >5 m (i.e. larger than exposed vertical section). Note that structures in (e) and (f) are taken ~20 m apart from each other and derive from the same fault (location 26).

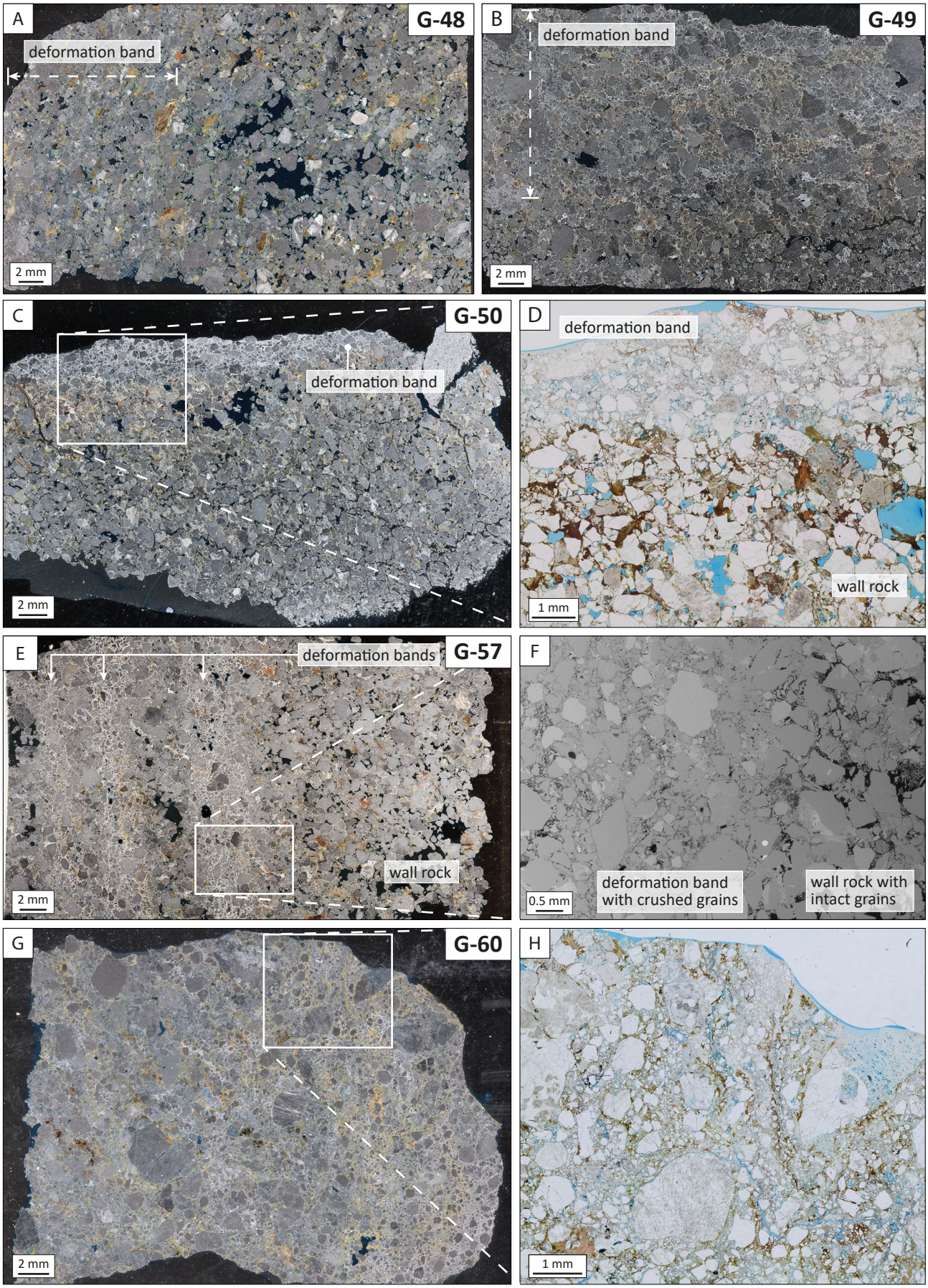

Fig. 5: Thin section photos of deformation bands. (a,b) samples G-48 and G-49 comprise deformation bands with low degree of cataclasis and subtle boundary to wall rock. (c,d) sample G-50 with deformation band showing a distinct boundary to the wall rock indicated by the brownish coloration of the latter; (e,f) sample G-57 exhibiting an array of three deformation bands; (g,h) sample G-60, deriving from the core of a cataclastic zone (figure 4f) showing intense grain fracturing and cataclasis in the whole thin section. Images a,c,e,g are taken in poralized incident ring light; d,h in plane-polarized light; f in backscattered electron. Large pores in all images are due to grain plucking during thin section preparation. For locations of samples in the outcrop see figure 4.

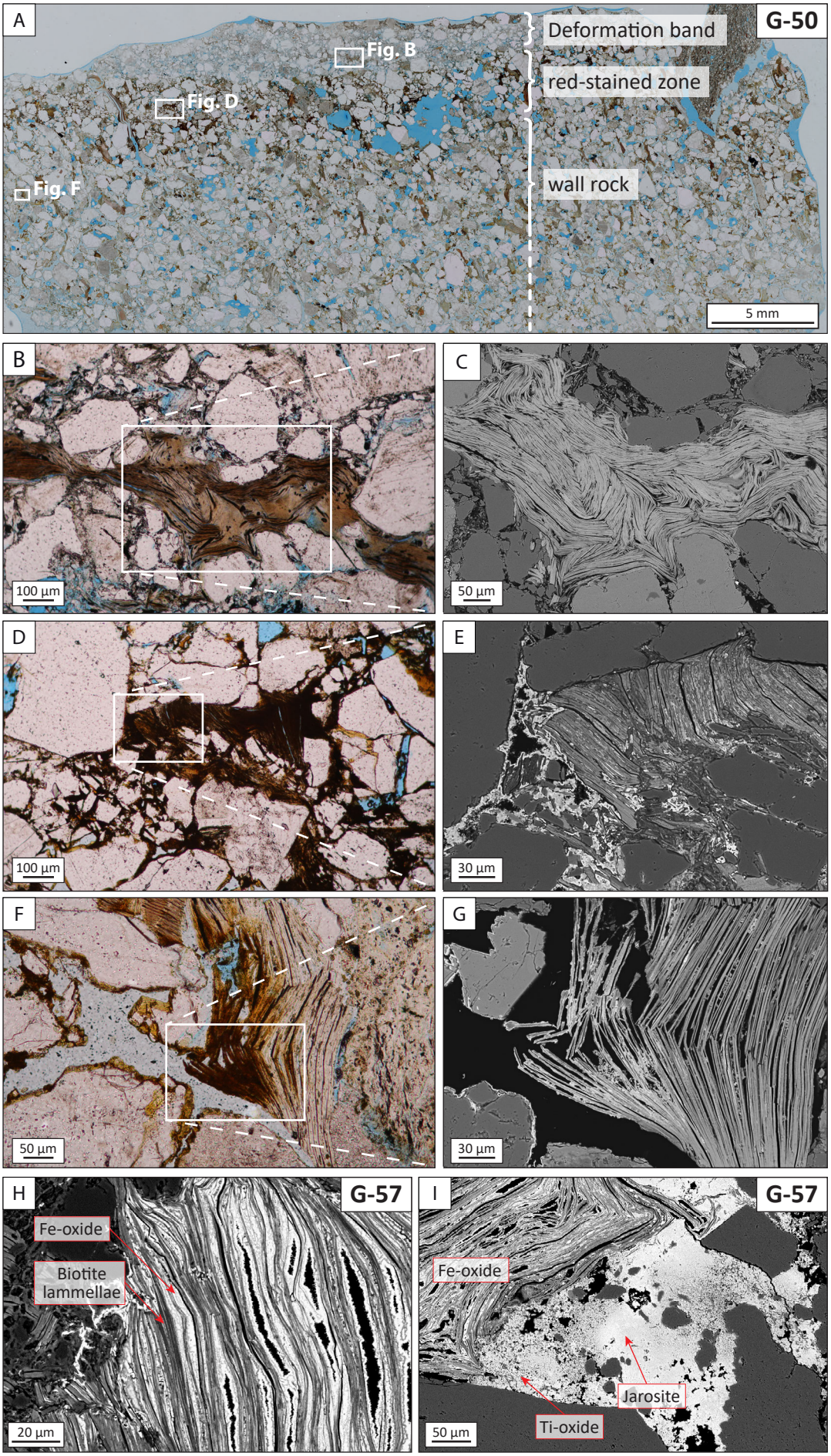

Figure 6: Thin section photos of deformation band and wall rock illustrating the degree of biotite alteration (a-g of sample G-50; h, i of sample G-57) in plane polarized light and backscatter electron imaging in and along the deformation band. (b,c) unaltered and intensively deformed biotite within deformation band; (d,e) altered and deformed and broken biotite lamellae with large quantity of Fe-oxides in red-stained zone; (f,g) slightly deformed biotite with alteration and oxide-precipitation restricted to delaminated part of biotite grain in wall rock; (h,i) intense Fe-, Ti-oxide, and jarosite precipitation within and near biotite grains in sample G-57 (EDX spectra and element maps in supplements S2).

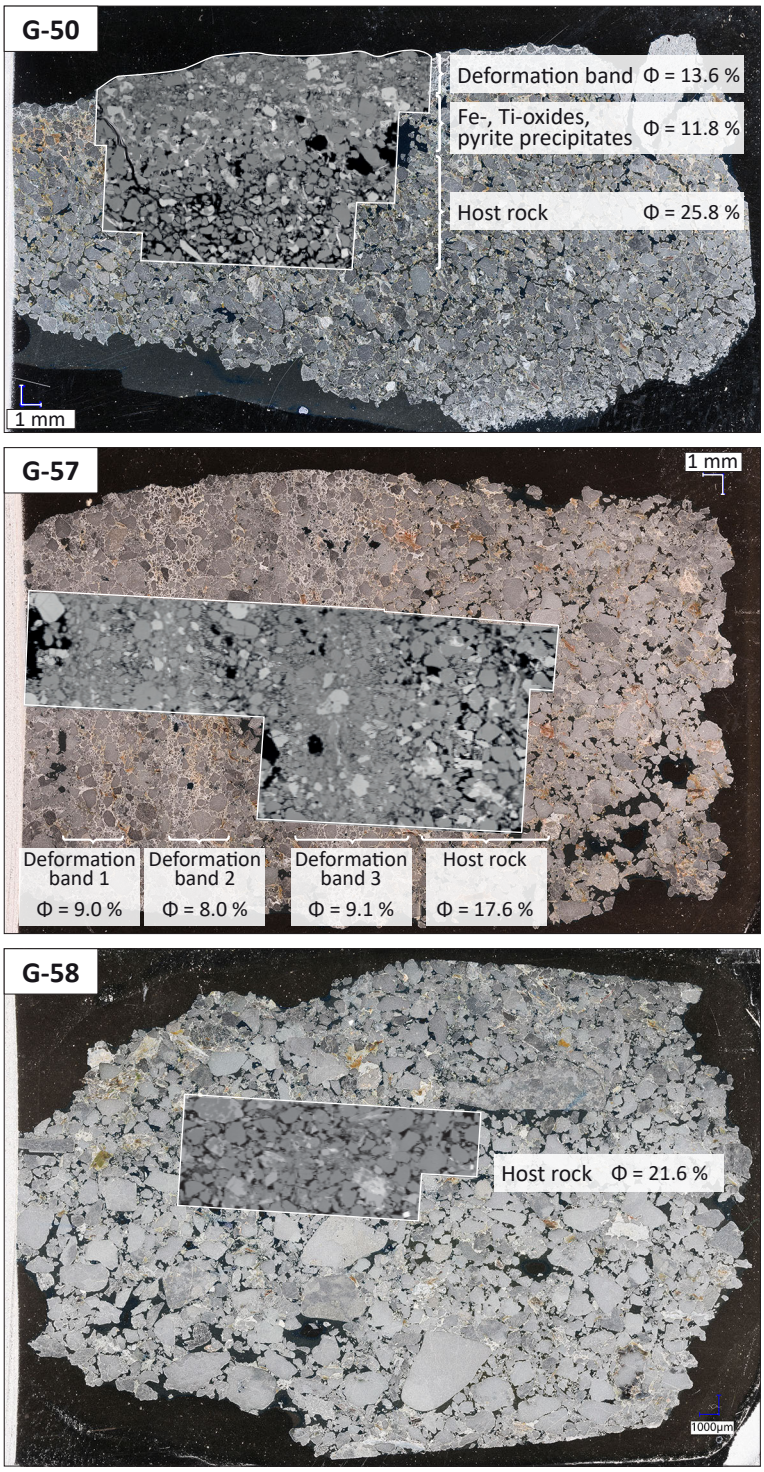

Fig. 7: Thin section photos of deformation bands (sample G-50, G-57) and host rock (sample G-58) with respective porosity values. Notice the porosity reduction from host rock to bands resulting from the cataclastic grain crushing. Porosity reduction also occurs along the bands, due to preferential precipitation of Fe- / Ti- oxides and pyrite (sample G-50). Sample G-58 is taken ~20 cm away from sample G-57 and has a porosity slightly higher than the host rock of G-57. This is in agreement with field appearance with a decrease in red staining away from the cluster of deformation bands. Porosity derived from 2-D image analysis of backscatter electron images (inset overlays in images).

Figure 8: Field photos illustrating the characteristics of veins cutting through cemented deposits. (a) surface of a vein fill consisting of blocky calcite; (b) vein fill consisting of multiple generations of microcrystalline calcite (location of sample G-9 thin section marked with white frame); (c) calcite vein with a thin rim of microcystalline calcite (sample G-10 derives from this vein, though exact location not in picture); (d) vein consiting of a microcrystalline calcite rim and an infill of microcrystalline calcite and sediment grains (sample G-13 derives from this vein, though exact location not in picture); (e) microcrystalline calcite infill succeeded by elongate calcite growth in upper part of vein (location of sample G-37 thin section marked with white frame). See figure 2 for location of photos.

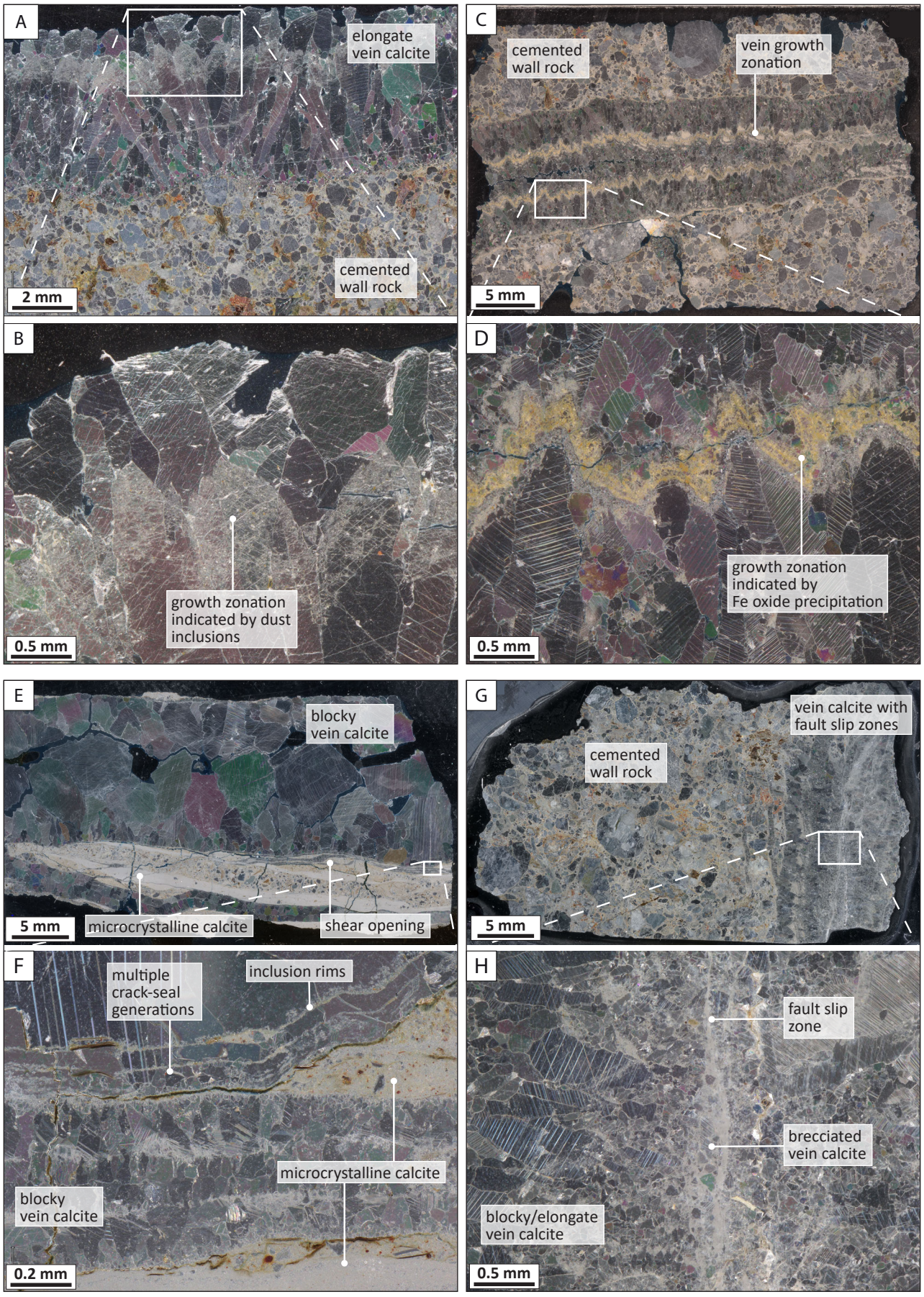

Figure 9: Thin section photos of calcite veins. (a,b) vein with growth generations that are distinguishable through the degree of dust inclusions; (c,d) vein exhibiting growth zonations with the inclusion of Fe-oxide precipitates; (e,f) vein exhibiting crack-seal texture with inclusion bands; light brownish material is microcrystalline calcite (see chapter 4.4 and figure 10 for detailed explanations); (g,h) vein comprising multiple fault slip zones. All images taken in polarized incident ring light.

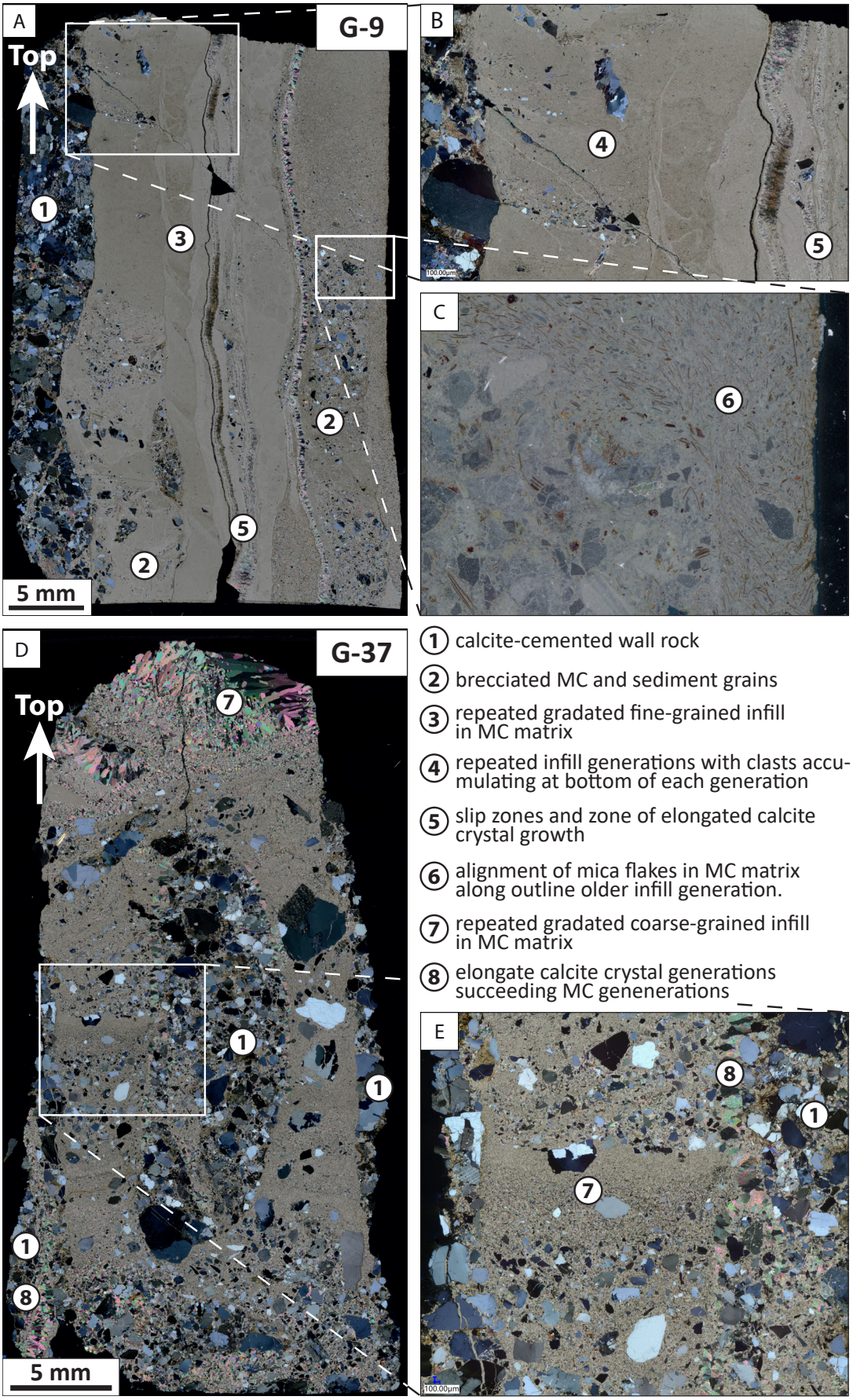

Figure 10: Thin section photos of three vein samples hosting microcystalline calcite (MC; light brownish mass in cross-polarized light) infill. (a-c) vertical face of sample G-9 shows an array of vein fill generations parallel to the wall rock. Within the generations a repeated gradation of upward fining infill is present. (d, e) vertical face of sample G-37 exhibits multiple generations of upward-fining vein fill, that are succeeded by elongate calcite crystal growth. (f) the horizontal face of sample G-13 shows a transition of vein fill from elongate calcite crystals to MC hosting lithic fragments. Main characteristics in thin sections are pointed out with numbers.

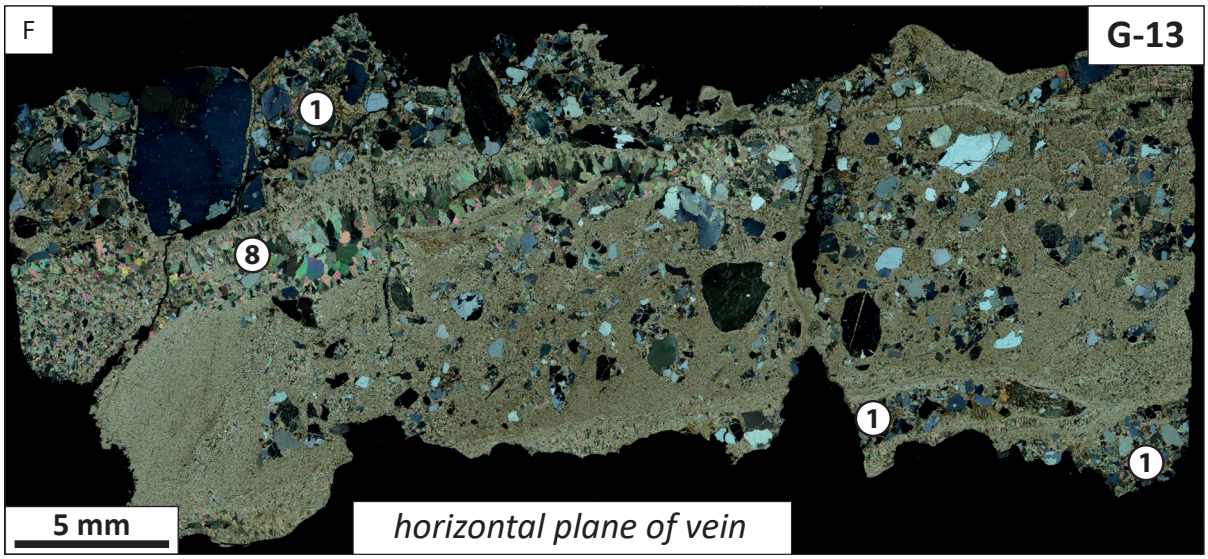

Figure 10: (continued).

a) Tectonic fracture opening in cemented sandstone and fluid injection due to fluid overpressure in uncemented sandstone. Precipitation of microcrystalline calcite from injected fluid.

b) Reduction of fluid overpressure and flow rate allows calcite and sediment clasts do settle at bottom of fracture. Turbulent fluid flow leads to heterogeneous spatial distribution of vein infll.

c) Renewed build-up of fluid overpressure may allow hydrofracturing leading to local brecciation of previous vein fill generations and a stacking of infill generations.

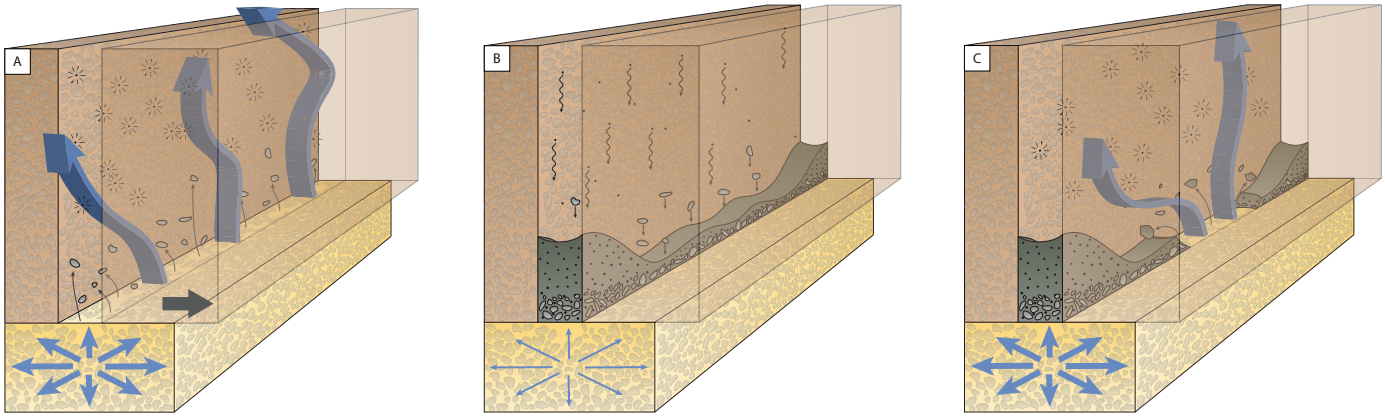

d) Alternatively, repeated tectonic fracture opening allows for the release of fluid overpressure and vertical parallel alignment of infill generation.

e) Moderate fluid pressure and saturation results in a more gradual super-saturation in the fracture and the precipitation of larger calcite crystals.

f) Finally, a vein has formed with elongate / blocky calcite succeding the precipitation of microcrystalline calcite.

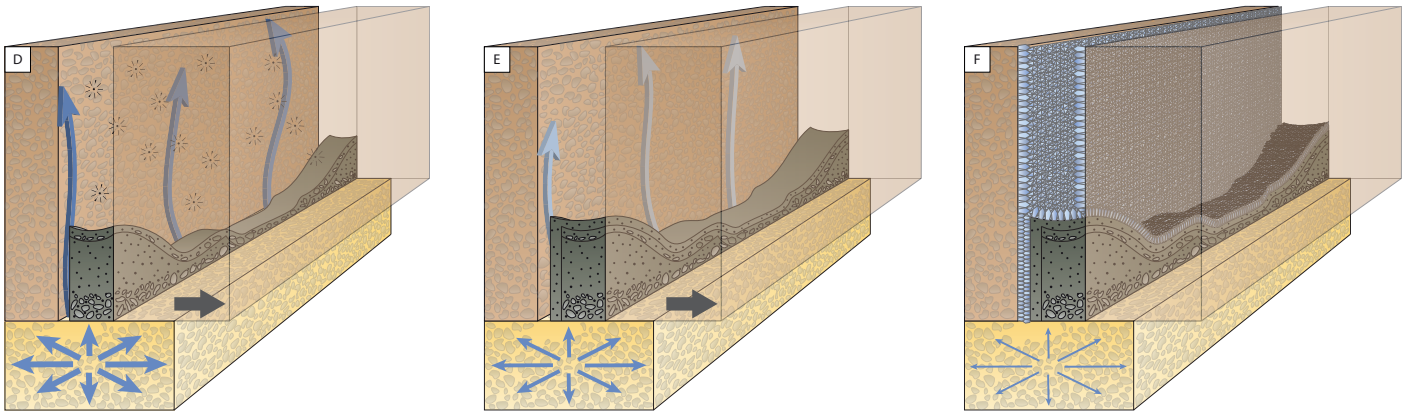

Figure 11: Conceptual model for the formation of microcrystalline calcite infill found in number of veins cutting through cemented sandstone within the cementation zone along the Dombjerg fault. The inferred main driver for the formation is initial calcite-saturated overpressured fluid in uncemented sandstone whose injection into a forming fracture is accompanied by sudden fluid pressure drop. This results in an instant super-saturation with respect to calcite and forces its quick precipitation.

Table 1: Porosity data of deformation band samples derived from BSE image analysis (cf. fig. 7).

Sample	ϕ wall rock	ϕ def band	ϕ alteration zone	Def band width	displacement
G-48	21.9	14.9	-	12.5 mm	0 cm
G-49	18.5	7.1	5.2	15.0 mm	5 cm
G-50	25.8*	13.6	11.8	1.5-3.0 mm	1-2 cm
G-57 / G-58	21.6	9.1 / 8.0 / 9.0	17.6	2-4 mm	n/a
G-60-2	-	8.8	-	> 250 mm	> 500 cm

* wall rock of G-50 suffered from expansion during impregnation.

Table 2: Carbon isotope values of microcrystalline calcite vein generations.

Sample	**$\delta^{13}C_{VPDB}$ ‰**
G-9g1	-13,56
G-9g2	-13,19
G-9g3	-13,41
G-10g1	-17,94
G-37g1	-16,19
G-37g2	-14,51